Paleoenvironmental fluctuations across the Jurassic–Cretaceous boundary from the Scotian margin, Canada

By

© Noelle Jia-Rong Lin

A thesis submitted to the School of Graduate Studies

In partial fulfillment of the requirements for the degree of

Master of Science

Department of Earth Sciences

Memorial University of Newfoundland

2023

St. John's, Newfoundland

ABSTRACT

Two wells, Thebaud C-74 and South Desbarres O-76 were investigated to evaluate paleoenvironmental changes during the Jurassic/Cretaceous boundary on the Scotian margin, offshore Nova Scotia. A multi-technique approach using several proxies of paleoredox, productivity, terrigenous input, and paleosalinity was employed, resulting in identification of a geochemical anomalies in both wells associated with the boundary. A shift to more reducing conditions and elevated productivity correlate with low terrigenous input at the start of the anomaly, followed by a shift of redox and productivity proxies back to background levels and elevated terrigenous input and paleosalinity. These correlative relationships are consistent in both wells, reflecting a transition to anoxic/euxinic conditions at the start of the anomaly that was predominantly driven by the consumption of oxidative agents due to a higher abundance of decomposing organic matter. The lack of correlation between productivity and terrigenous input indicates that the increase in micronutrients driving elevated productivity is not related to an influx of terrigenous input, but rather upwelling. The positive correlation between terrigenous input and paleosalinity suggests limited fluvial input. These results agree with global paleoclimate and sealevel variations during the Late Jurassic/Early Cretaceous and reflect semi-arid/arid conditions related to relative sealevel fall and open ocean circulation as the North Atlantic Ocean expanded.

GENERAL SUMMARY

Studying the chemistry of the ancient ocean is a valuable tool in understanding and reconstructing fluctuations in environmental factors such as oxygen, photosynthesis, input of continental materials into the ocean, and salinity, all of which provide insight into what the Earth and oceans were like 145 million years ago. This study analyzes the trace element composition of mudrock and sandstone from offshore Nova Scotia through the evaluation of two wells, Thebaud C-74 and South Desbarres O-76, which span the Jurassic–Cretaceous boundary. The objective of this study is to understand what the oceanic environmental conditions were like during this time, how they changed, and how this is related to documented regional and global changes. The results identify a geochemical anomaly in both wells that indicates shifts in the regional paleoclimate drove shifts in oceanic circulation and chemistry, affecting biotic communities across this time interval.

ACKNOWLEDGEMENTS

I would like to thank my supervisors, Drs. Karem Azmy and Nikole Bingham-Koslowski, for their guidance and support throughout this entire project. I am extremely grateful for the opportunity to move to Newfoundland and work on a project that I am passionate about. I'd also like to thank Drs. J, Potter, Geert van Biesen, and B. Guégen for their help with the geochemical analyses. Thank you to Dr. Jennifer Galloway (GSC) for completing the internal review. I would also like to thank Sam Nicoll from the C-NSOPB for her time and patience in the sample collection process. This project was supported by Net Zero Atlantic, the C-NSOPB, the Geological Survey of Canada (Atlantic), and the Nova Scotia Department of Natural Resources and Renewables.

Thank you to my parents and to Jake Herrmann for the unconditional support, love, and advice, and for showing me that good things come to those who work hard. This project would not have been possible without the support of these people.

CO-AUTHORSHIP STATEMENT

The thesis is presented in the traditional format. The design and identification of the research project were outlined by Drs. Karem Azmy and Nikole Bingham-Koslowski, who guided and advised my progress throughout the project and corrected the written manuscript prior to submission. Aside from sample collection and laboratory analysis, all aspects of the thesis were my responsibility as primary author. This includes the literature review, selection of wells and sampling depths, refining of objectives, laboratory preparations, data analysis and interpretation, and assembly of the manuscript. A paper manuscript titled "Paleoenvironmental fluctuations across the Jurassic–Cretaceous boundary from the Scotian margin, Canada" is currently under review to be published in "Palaeogeography, Palaeoclimatology, Palaeoecology". Sample collection was completed by Sam Nicoll from the C-NSOPB, C and N laboratory analysis was completed by Drs. Joanna Potter and Geert van Biesen at Memorial University of Newfoundland, and elemental analysis was completed by Dr. Bleuenn Guégen at Pôle de Spectrométrie Océan, IUEM, Brest, France.

TABLE OF CONTENTS

LIST OF FIGURES

$_{Crust}$), Zn (EF_{PAAS}), Al, Ti, Al/Ti, K/Al, and ∑REE of the South Desbarres O-76 well. The black dots mark the stratigraphic levels of the collected samples. Grey shading represents the geochemical anomaly. Stratigraphic boundaries based on biostratigraphy from Weston et al., 2012. Lithology based on Sine et al., 1984.

Figure 4.1: $\delta^{13}C_{org}$ vs TOC and $\delta^{15}N_{air}$ vs TOC for the Thebaud C-74 and South Desbarres O-76 wells.

Figure 4.2: Summary of organic isotope data for the Jurassic–Cretaceous from Atlantic, Arctic, and Tethyan sections (modified from Galloway et al., 2020). Red stars indicate levels interpreted as VOICE by Turner et al., 2019.

LIST OF TABLES

LIST OF ABBREVIATIONS AND SYMBOLS

TOC: total organic carbon

TON: total organic nitrogen

∑REE: total rare earth elements

J/K: Jurassic–Cretaceous

GSSP: Global Boundary Stratotype Section and Point

OM: organic matter

EF: enrichment factor

PAAS: Post-Archean-Australian Shale

C-NSOPB: Canada-Nova Scotia Offshore Petroleum Board

NBCU: Near Base Cretaceous Unconformity

MUN: Memorial University of Newfoundland

PSO: Pôle de Spectrométrie Océan

VOICE: Volgian Carbon Isotope Excursion

LIST OF APPENDICES

1

CHAPTER 1

INTRODUCTION

1.1. General Introduction

Trace element and isotope geochemistry of sedimentary rocks are useful tools for the interpretation and evaluation of paleoenvironments. The variations of trace elements and elemental ratios in siliciclastic rocks can be used as reliable proxies of paleoredox conditions (e.g., total organic carbon (TOC), total organic nitrogen (TON), U, V, Mo, Cr, Fe, Mn, Th/U), bioproductivity patterns (e.g., $\delta^{13}C_{org}$, $\delta^{15}N_{air}$, TOC, TON, Ni, Cu, P, Zn), weathering source material composition (e.g., Al, Ti, Al/Ti, K/Al, total rare earth elements (∑REE)), and fluctuations in paleosalinity (e.g., B/Ga) (Wignall and Myers, 1988; Hatch and Leventhal, 1992; Calvert and Pederson, 1993; Jones and Manning, 1994; Schnetger et al., 2000; Piper and Perkins, 2004; Rimmer, 2004; Jiang et al., 2006; Lyons and Severmann, 2006; Tribovillard et al., 2006; Perkins et al., 2008; Algeo and Tribovillard, 2009; Piper and Calvert, 2009; Poulton et al., 2010; Śliwiński et al., 2010; Zhou et al, 2012; Pattan et al., 2013; Mortazavi et al., 2014; Tripathy et al., 2014; Sabatino et al., 2015; Gao et al., 2016; Wang and Azmy, 2020; Shembilu and Azmy, 2022).

The Scotian margin has been widely studied, with 130 exploration wells drilled, ultimately yielding several major oil and gas discoveries. Petroleum exploration began in 1958 by Mobil Oil Canada Ltd and a formal study for hydrocarbon resource potential was conducted by the Geological Survey of Canada in 1972. The stratigraphy of this region appears to be continuous across a large geographic area as described by Jansa and Wade (1975), who, building on earlier studies (e.g., McIver, 1972; Amoco Canada Petroleum Company Limited and Imperial Oil Limited, 1973), proposed a Mesozoic–Cenozoic stratigraphy of the Scotian Shelf and Grand

Banks of Newfoundland. The current biostratigraphy of the region is recognized through the improved biozonation in offshore wells based on Ascoli's (1976) study of foraminifera and ostracods, and Williams' (1975) and Barss' et al. (1979) work with palynomorphs. Additionally, an updated biostratigraphic scheme was produced by Weston et al., (2012) that uses a multi-faceted approach with nannofossils, palynomorphs, and microfossils.

Major stratigraphic boundaries generally occur during periods of significant environmental, biological, and/or lithological fluctuation, and are defined by a Global Boundary Stratotype Section and Point (GSSP). The Jurassic–Cretaceous (J/K) boundary, however, has not yet been ratified with a GSSP as it is typically obscured in strata due to widespread fossil provincialism during this period, as well as a lack of major glacio-eustatic fluctuations, or global change in lithology (Barragán et al., 2020; Dzyuba et al., 2013; Remane, 1991; Scott, 2019; Tennant et al., 2017; Wimbledon, 2008). Galloway et al. (2020) studied the Volgian Carbon Isotope Excursion (VOICE) in the Sverdrup Basin of Arctic Canada and documented a global occurrence of a negative isotopic excursion event that is also present in the North Sea (Turner et al., 2019), Norway (Hammer et al., 2012; Koevoets et al., 2016), Siberia (Zakharov et al., 2014), the United Kingdom (Morgans-Bell et al., 2001), and Argentina (Capelli et al., 2020). This event is linked to global low sealevel (e.g., Price et al., 2016; Barragan et al., 2020; Martínez-Yáñez et al. 2017; Michalik et al., 1995; Grabowski et al., 2010), extensive anoxic bottom waters and open oceanic circulation (Martínez-Yáñez et al., 2017; Price et al., 2016; Barragan et al., 2020), and semi-arid to arid conditions (Föllmi, 2012; Price et al., 2016; Grabowski et al., 2017; Haq, 2017; Barragán et al., 2020; Capelli et al., 2020). Numerous studies have been conducted along the Scotian margin to identify source rocks for petroleum exploration, indicating significant Tithonian aged source rocks that are well defined, organic-rich, and mature (Offshore Energy Technical Research Association, 2011). As such, chemostratigraphic analyses on strata that span

the J/K boundary on the Scotian margin can provide valuable information needed to constrain paleo-oceanographic and environmental changes related to source rock deposition, and ultimately contribute to constraining and ratifying the J/K GSSP.

In the current study, a wide range of proxies, including $\delta^{13}C_{org}$, $\delta^{15}N_{air}$, TOC, TON, and trace elements, are applied to siliciclastic sedimentary rocks from offshore Nova Scotia spanning the J/K boundary (Tithonian to Valanginian). This is accomplished through the geochemical analyses of core samples, supplemented by cuttings collected at high resolution (1 m or less) from the Thebaud C-74 (60°11'35.62" W 43°53'5.34" N) and South Desbarres O-76 (59°55'59.02" W 44°5'56.07" N) wells (Fig. 1.1). These two wells were selected based on core photographs and biostratigraphic, lithological, and geochemical reports available through the Canada-Nova Scotia Offshore Petroleum Board (C-NSOPB). The wells were selected targeting organic rich mudrock, and availability of accurate biostratigraphic and palynology studies (e.g., Weston et al., 2012; Ascoli, 2004; Williams, 1975) indicating the depth range at which the J/K boundary likely occurred. The results of this study are expected to significantly contribute to the Nova Scotia geochemical database and assist with the reconstruction of the depositional environments, including organic-rich mudrocks that can form economically important hydrocarbon source rocks.

The ultimate purpose of the investigation is to evaluate whether paleoenvironmental changes occurred in the strata that span the Jurassic–Cretaceous boundary on the Scotian margin. A multi-geochemical proxy approach technique is applied to better understand the changes in paleoredox conditions, and to investigate the variations in productivity, terrigenous input, redox, and paleosalinity conditions of the Scotian Basin during a time of global change across the J/K boundary.

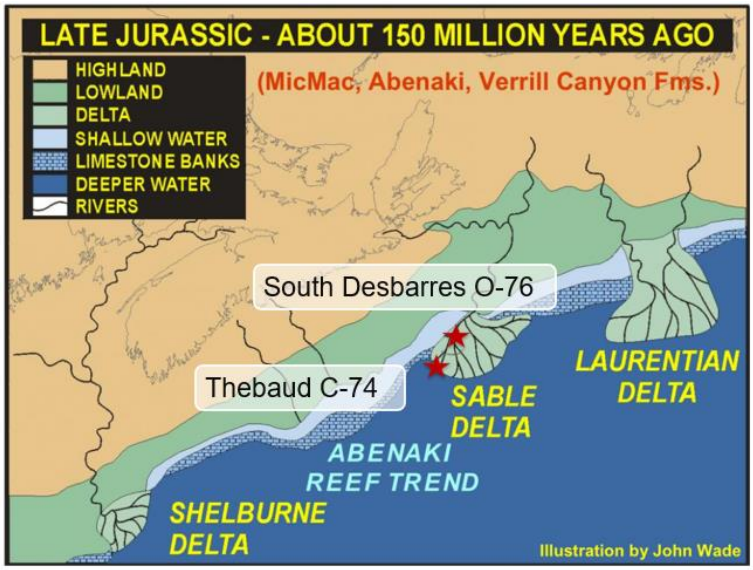

Figure 1.1. A simplified paleogeographic reconstruction of the Scotian Basin during the Late Jurassic, with approximate well locations of Thebaud C-74 and South Desbarres O-76 (modified from Wade, 2012).

1.2. Paleoenvironmental Geochemical Proxies

1.2.1. Paleoredox

Paleoredox studies aim to track the distribution of oxidizing agents and distinguish the biogeochemical processes that influence them (Tribovillard et al., 2006). A multi-proxy approach with elements that predictably respond to redox variations, such as Mo, V, U, Cr, Fe, Mn, and Th/U (e.g., Tribovillard et al., 2006; Śliwinski et al., 2010; Wignall et al., 2007; Wignall and Twitchett, 1996; Algeo and Maynard 2004), is used to identify a full spectrum of redox conditions, including oxic, suboxic, anoxic (without free H_2S), and euxinic conditions.

Molybdenum is mainly present in seawater as molybdate (MoO_4^{2-}; Broecker and Peng, 1982). It is not easily adsorbed by natural particles or clay minerals, or concentrated by ordinary plankton (Brumsack, 1989), however it is easily captured by Mn-oxyhydroxides at the sediment surface (Bertine and Turekian, 1973; Calvert and Pederson, 1993; Zheng et al., 2000). Reduction of these phases liberates adsorbed Mo to pore waters, enhancing Mo enrichment in the shallow

burial realm (Crusius et al., 1996). The most significant driver of Mo enrichment is the presence of free sulfide (H_2S) in anoxic environments, via the molybdate to thiomolybdate conversion, or sorption/precipitation of Mo to Fe-sulfides (Algeo and Lyons, 2006; Erickson and Helz, 2002; Bennett and Canfield, 2020). Thiomolybdate is particle-reactive and prone to scavenging, so once the conversion has taken place, Mo is scavenged by bonding with metal-rich (Fe) particles, sulfur-rich organic molecules, and iron sulfides (Helz et al., 1996; Tribovillard et al., 2006). Authigenic Mo concentrations are useful as a paleoredox proxy in identifying the presence of free H_2S when compared with other independent paleoredox proxies.

Vanadium is present in oxic water as V(V), which readily adsorbs onto Mn- and Fe-oxyhydroxides (Calvert and Piper, 1984; Wehrly and Stumm, 1989; Tribovillard et al., 2006). Mildly reducing conditions causes V(V) to be reduced to V(IV), forming vanadyl ions (Emerson and Huested, 1991). In euxinic conditions, the presence of free H_2S released by bacterial sulfate reduction causes further reduction to V(III) (Tribovillard et al., 2006). This two-step reduction of V results in distinct solubilities under non-sulfidic anoxic and euxinic conditions (Calvert and Pederson, 1993; Algeo and Maynard, 2004; Tribovillard et al., 2006).

In oxic marine settings, U is mainly present as dissolved U(VI) as uranyl ions, where it is not reduced to U(IV) or scavenged by particulates (Anderson et al., 1989; Tribovillard et al., 2006). Uranium(VI) reduction to U(IV) takes place in the sediment via diffusion of $UO_2(CO_3)_3^{4-}$ from the water column, reduction reactions, and adsorption of precipitate as UO_2, U_3O_7, or U_3O_8 (Crusius et al., 1996; Zheng et al., 2000; Chaillou et al., 2002; Tribovillard et al., 2006), and is not directly influenced by redox cycling of Fe and Mn in the water column (Algeo and Maynard, 2004; McManus et al., 2005; Tribovillard et al., 2006). Bacterial sulfate reduction reactions accelerate U accumulation (Zheng et al 2002a, b; McManus et al., 2005), while oxygen

penetration depth and sedimentation rate influences the rate of diffusion of uranyl ions from the water column to the sediment (Crusius and Thomson, 2000). Conversely, Th occurs permanently as insoluble Th(IV) in all redox conditions in the water column. Anoxic environments in which U is enriched will yield a lower Th/U (<2) ratio than oxic environments (>2), making it a reliable paleoredox proxy (Wignall and Twitchett, 1996). Chromium is present as soluble Cr(VI) in oxic seawater, and reduced to Cr(III) in reducing environments. Due to structural and electronic incompatibilities, Cr(III) is not readily trapped within the sediments in the form of insoluble sulfides (Tribovillard et al., 2006; Morse and Luther, 1999).

Iron and Mn also reflect changes in redox conditions due to their higher solubility in reducing conditions, causing them to be enriched in suboxic and anoxic environments (Landing and Bruland, 1987). They also play an important role in transporting trace elements from the water column to the sediment, primarily influencing Ni, Cu, Zn, Co, Pb, Mo, V, and Cr due to their affinity to adsorb onto the surface of Fe-Mn oxyhydroxides. These elements are then exported to the sediment and released by reductive dissolution, making them available for new reactions (Tribovillard et al., 2006).

1.2.2. Productivity

Isotopic signals such as $\delta^{13}C$ and $\delta^{15}N$, as well as trace element concentrations such as Ni, P, Cu, and Zn can be evaluated as a suite of proxies representative of organic productivity (e.g., Calvert and Pederson, 1993; Tribovillard et al., 2006; Piper and Calvert, 2009; Śliwinski et al., 2010; Wang and Azmy, 2020). Nickel, Cu, P, and Zn behave as micronutrients utilized by the growing phytoplankton, which sink to the seafloor as particulate organic matter (OM) settles, ultimately transporting these trace elements below the photic zone (Piper and Calvert, 2009). These nutrients are supplied to the ocean via freshwater input from rivers or groundwater and

atmospheric deposition and cycled within the ocean via upwelling and mixing of subsurface and surface waters (Piper and Calvert, 2009).

Carbon is the primary element in the biosphere and exists as two naturally occurring stable isotopes: the lighter ^{12}C, and the heavier ^{13}C. The $\delta^{13}C_{org}$ isotopic depletion indicates an enrichment in the isotopically lighter ^{12}C, which is caused by higher levels of photosynthesis and, thus, productivity (Hoefs, 2004; Faure and Mensing, 2004). During photosynthesis, plants preferentially absorb $^{12}CO_2$ molecules via diffusion through the cell membrane because it is more easily metabolized than the isotopically heavier $^{13}CO_2$ (Hoefs, 2004; Faure and Mensing, 2004). Total organic carbon and TON values can reflect both productivity levels resultant from OM generation, and/or bottom-water oxygen, where accumulation reflects reducing conditions driving preservation of OM (Canfield, 1994; Murphy et al., 2000; Schoepfer et al., 2014).

$\delta^{15}N_{air}$ has historically been used as a proxy for paleoredox conditions and the source of organic matter (Altabet and Francois, 1994; Yamaguchi et al., 2010; Quan et al., 2013; Wang and Azmy, 2020). Nitrogen has two stable isotopes: ^{15}N and ^{14}N. Like $\delta^{13}C_{org}$, photosynthetic processes favour the isotopically lighter ^{14}N in the form of $^{14}NO_3^-$, causing phytoplankton to have lower $\delta^{15}N$ values (Altabet and Francois, 1994). Isotopic N concentrations are also heavily influenced by microbial denitrification, which results in the reduction of NO_3^- to N_2 in oxygen-depleted waters, and enrichment of ^{15}N in organic matter (Cremonese et al., 2013; Quan et al., 2013; Wang and Azmy, 2020). This can cause significant local enrichment of subsurface nitrate (Cline and Kapan, 1975), which can influence interpretations of productivity when evaluating the $\delta^{15}N$ signal. Generally, the $\delta^{15}N$ signal is preserved in organic matter that rains down from the surface water, and the recorded variations in the signal from surface NO_3^- is a function of phytoplankton nutrient depletion (Wada, 1980; Altabet and Francois, 1994).

1.2.3. Terrigenous Input

The geochemical composition of siliciclastic sediments is controlled largely by lithology of the sediment source, weathering, transport, and diagenetic processes (Dobrzinski et al., 2004; Detian et al., 2019). A large contribution of trace elements into the ocean is the result of terrestrial weathering and consequential runoff of siliciclastic debris, which is a process that can be modelled using terrigenous input proxies such as Al, Ti, Al/Ti, K/Al and ∑REEs (e.g., Piper and Calvert, 2009; Śliwinski et al., 2010; McLennan et al., 1980; Wang and Azmy, 2020). Understanding the degree of terrestrial input into the ocean is an important consideration in paleoenvironment reconstruction due to the trace element concentrations that can be influenced by detrital flux.

Aluminum concentrations are an indicator of the aluminosilicate fraction of the sediment, and are known to be immobile during diagenesis and, therefore, a reflection of detrital input (Brumsack, 1989; Calvert and Pederson, 1993; Piper and Perkins, 2004; Tribovillard et al., 2006). Titanium and ∑REEs are also enriched in crustal rocks, and therefore reflect the input of terrestrial input into the ocean (McLennan et al., 1980; McLennan, 2001; Śliwinski et al., 2010; Wang and Azmy, 2020). Sealevel fall causes more land to be exposed and thus, an increase in terrestrial weathering and detrital material transported to the ocean, which is reflected in positive Al, Ti, Al/Ti, and ∑REE profiles (Piper and Perkins, 2004; Śliwinski et al., 2010). These profiles can be compared and correlated with other proxies to infer relative sealevel change, which directly influences oxygen levels in the water column and productivity levels (Wang and Azmy, 2020).

The K/Al is an indicator of variation in the abundance of illite, a non-expansive clay mineral that is associated with diagenesis of siliciclastic sediments in continental environments

and is typically recycled as detrital sediments (Sabatino et al., 2015). High K/Al (>0.3) ratios are associated with the presence of illite supplied as detrital sedimentary components, while low K/Al ratios (<0.3) are linked to the presence of clay minerals with low K (such as kaolinite), which is associated with enhanced hydrolysis in humid climates (Sabatino et al., 2015).

1.2.4. Paleosalinity

Paleosalinity analysis is a useful tool in determining the degree of freshwater or marine input, which can be paired with paleogeographic considerations and geochemical proxies to provide additional insight on the depositional environments of ancient marginal marine systems (Wei and Algeo, 2020). The B/Ga ratio is a useful paleosalinity proxy due to the differential concentration of B and Ga in seawater and freshwater. A B/Ga ratio >6 indicates more marine conditions, a moderate B/Ga ratio (3 to 6) indicates brackish water, and a low B/Ga ratio (<3) indicates freshwater conditions (Wei and Algeo, 2020).

The main objectives of the current investigation are:

- Better understand the changes in paleoredox conditions using variations in TOC, TON, U, V, Mo, Cr, Fe, Mn, and Th/U signatures,
- Investigate the variations in the bioproductivity proxies in the Scotian Basin ($\delta^{13}C_{org}$, $\delta^{15}N_{air}$, TOC, TON, Ni, Cu, P, and Zn) and the impact of paleoredox variations on these proxies
- Examine terrigenous inputs in the region during this time through elemental (e.g., Al, Ti, Al/Ti, K/Al) and ∑REE analyses, and
- Investigate fluctuations in paleosalinity using the elemental ratio B/Ga.

1.3. Geological Setting

The investigated interval was deposited along the Scotian margin, offshore Nova Scotia, Canada, in the Scotian Basin which extends ~1200 km from the eastern part of Georges Bank to the Central Grand Banks (Figs. 1.2, 1.3). The Scotian Basin is flanked by the Yarmouth Arch to the southwest and the Avalon Uplift to the northeast where it underpins both the Scotian Shelf and Scotian Slope. Directly north of the basin are the uplands of Nova Scotia and Newfoundland and the Sydney Basin, with the LaHave Platform to the northwest (Fig. 1.2; Jansa and Wade, 1975). The Scotian Basin consists of Mesozoic–Cenozoic sediments associated with the development of the North Atlantic Ocean Basin (Wade and MacLean, 1990b). It is divided into a series of interconnected sub-basins, namely the Shelburne, Sable, Abenaki, Laurentian, and South Whale sub-basins (Wade and MacLean, 1990b). These sub-basins are part of an extensive system of basins that extend from the southeastern United States to northern Baffin Bay that formed during the rifting of Pangea and the opening of the Atlantic Ocean. Up to 18 km of Mesozoic and Cenozoic strata accumulated within these Scotian margin sub-basins as a result of prolonged subsidence. Salt distribution throughout these sub-basins suggests the possibility of evaporite and redbed deposition during the prerift to early synrift phases (Wade and MacLean, 1990b). Each of the sub-basins experienced different rates of sediment accumulation and storage, driven by interactions between sediment supply and subsidence (Deptuck and Kendell, 2017).

The Scotian Shelf originated ~200 Ma as part of a passive margin off the coast of eastern North America during the breakup (Wilson Cycle) of the supercontinent Pangea as the African plate separated from its North American counterpart (Labails et al., 2010; Sibuet et al., 2011). The first stage of the Wilson Cycle eventually resulted in the opening of the North Atlantic, separating the Appalachian-Caledonian Orogen. At this time, eastern Canada was in the middle of Pangea, where early rift basins developed along the structural grain of Paleozoic crust

produced by complex earlier periods of tectonic deformation (Swanson, 1986). This framework included the Appalachian Mountains in the south and the Canadian Shield in the north (Keen and Piper, 1990). The breakup process began with a rift phase in the Middle Triassic, followed by the onset of seafloor spreading in the Early Jurassic and drift phase of basin development. The Paleozoic basement rocks consist of the lower Paleozoic Avalon and Meguma terranes of the Avalon Orogen, separated by the Chedabucto fault zone across northern Nova Scotia and its extension into southern Newfoundland (Fig. 1.2; Schenk, 1971; Williams, 1979; Marillier et al., 1989; Wade and MacLean, 1990b; MacLean and Wade, 1993). The Scotian Shelf is a major morphological element of the Canadian Atlantic continental margin (Fig. 1.3), situated directly southeast of Nova Scotia and covering 960 000 km^2 (Wade and MacLean, 1990a). It can be subdivided into three physiographic zones: (1) the inner zone, an area of rough topography spanning from the shoreline to the edge of the coastal plains; (2) the middle zone, a series of broad basins and deep irregular channels caused by ancient drainage courses; and (3) the smooth and sandy outer zone (Wade and MacLean, 1990a).

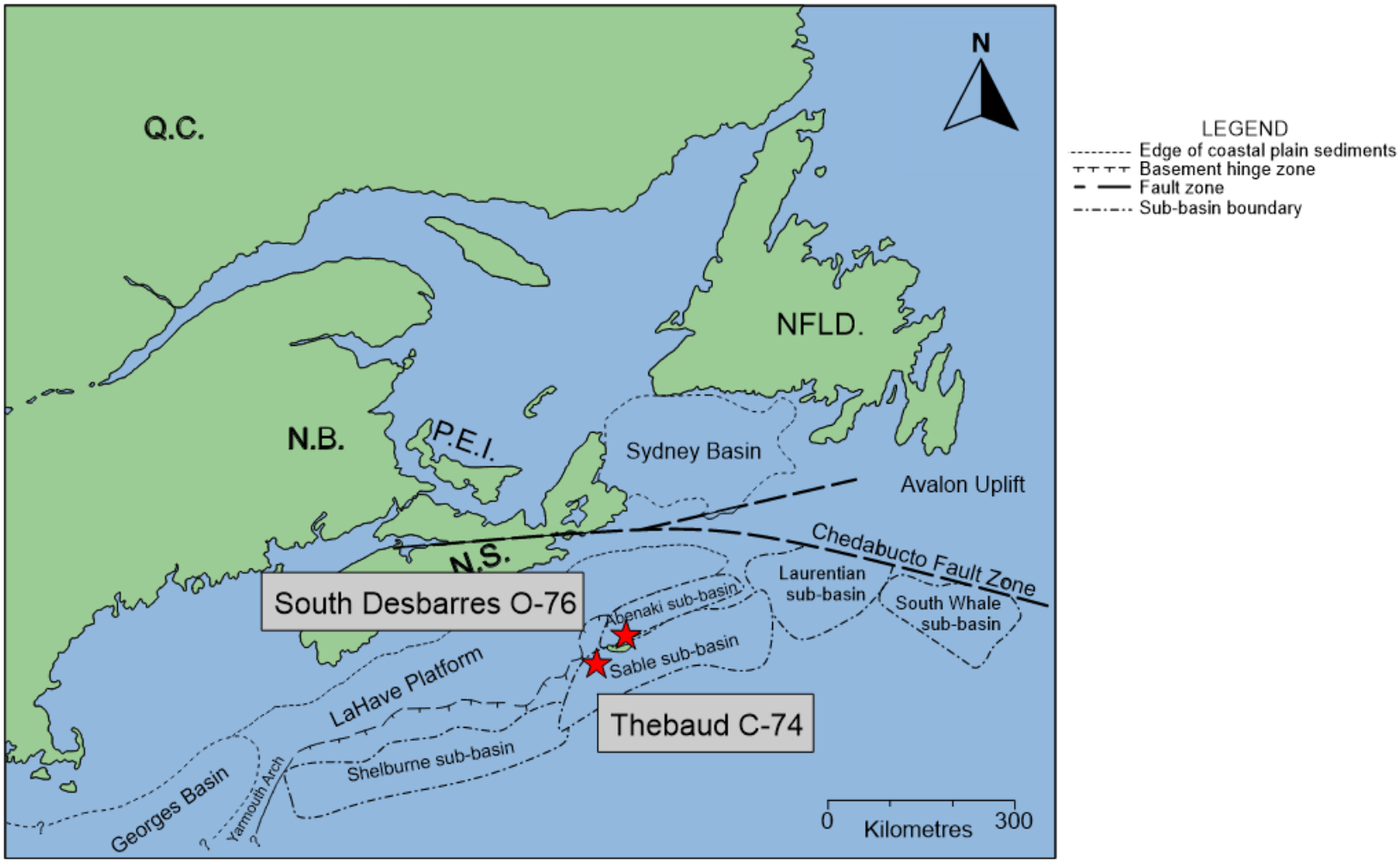

Figure 1.2. Regional map of the research area showing major morphological elements of the Scotian Basin (modified from Weston et al., 2012; Jansa and Wade, 1975; Beicip-Franlab, 2014).

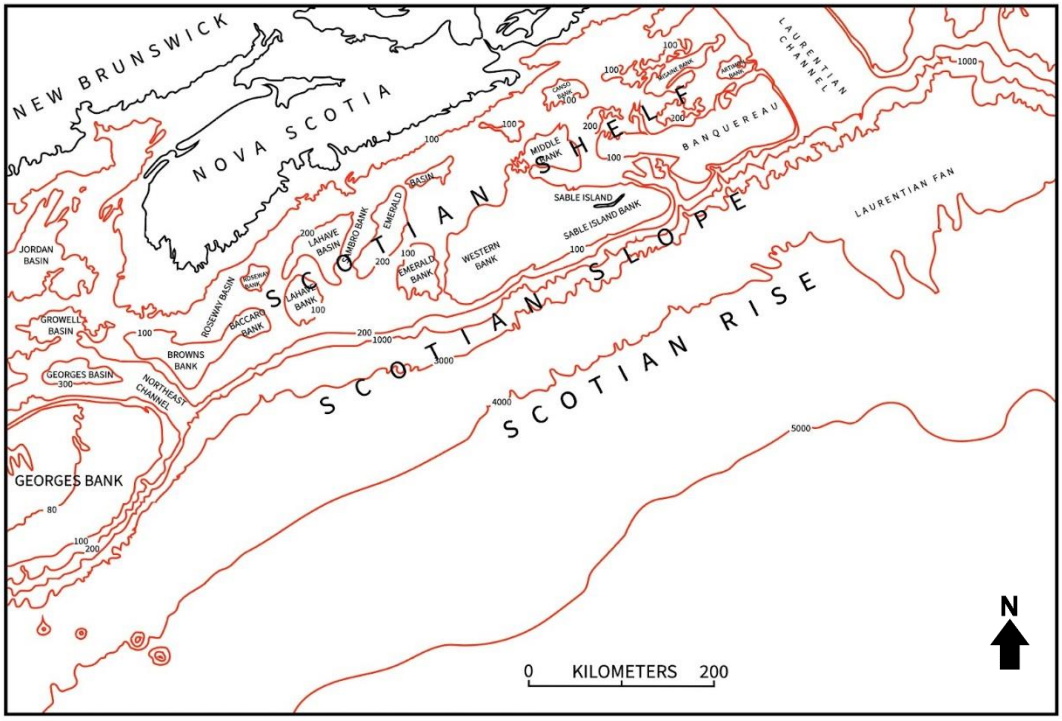

Figure 1.3. Physiography of the Scotian Shelf. Lines are bathymetric contour lines with depths stated in metres (modified from Wade and MacLean (1990a)).

In the Scotian Basin, Mesozoic and Cenozoic strata overlie locally older Paleozoic rocks (Fig. 1.4; Pe-Piper and Jansa, 1999), where there is proven economic petroleum (Wade and MacLean, 1990a). The post-Paleozoic strata are composed of both synrift and postrift packages, which are separated by a prominent regional breakup unconformity (Wade et al., 1995). The oldest Mesozoic strata known from the Scotian Basin are Middle Triassic in age and consist of red clastics of the Eurydice Formation and the coeval evaporites of the Argo Formation (Fig. 1.4; Wade and MacLean, 1990b). Later remobilization of synrift salt produced a variety of salt bodies on the slope (Slope Diapiric Province) that disrupt the sedimentary section. Salt movement also produced large synsedimentary faults present in the sedimentary sections, particularly within the Abenaki and Sable subbasins (Wade et al., 1995).

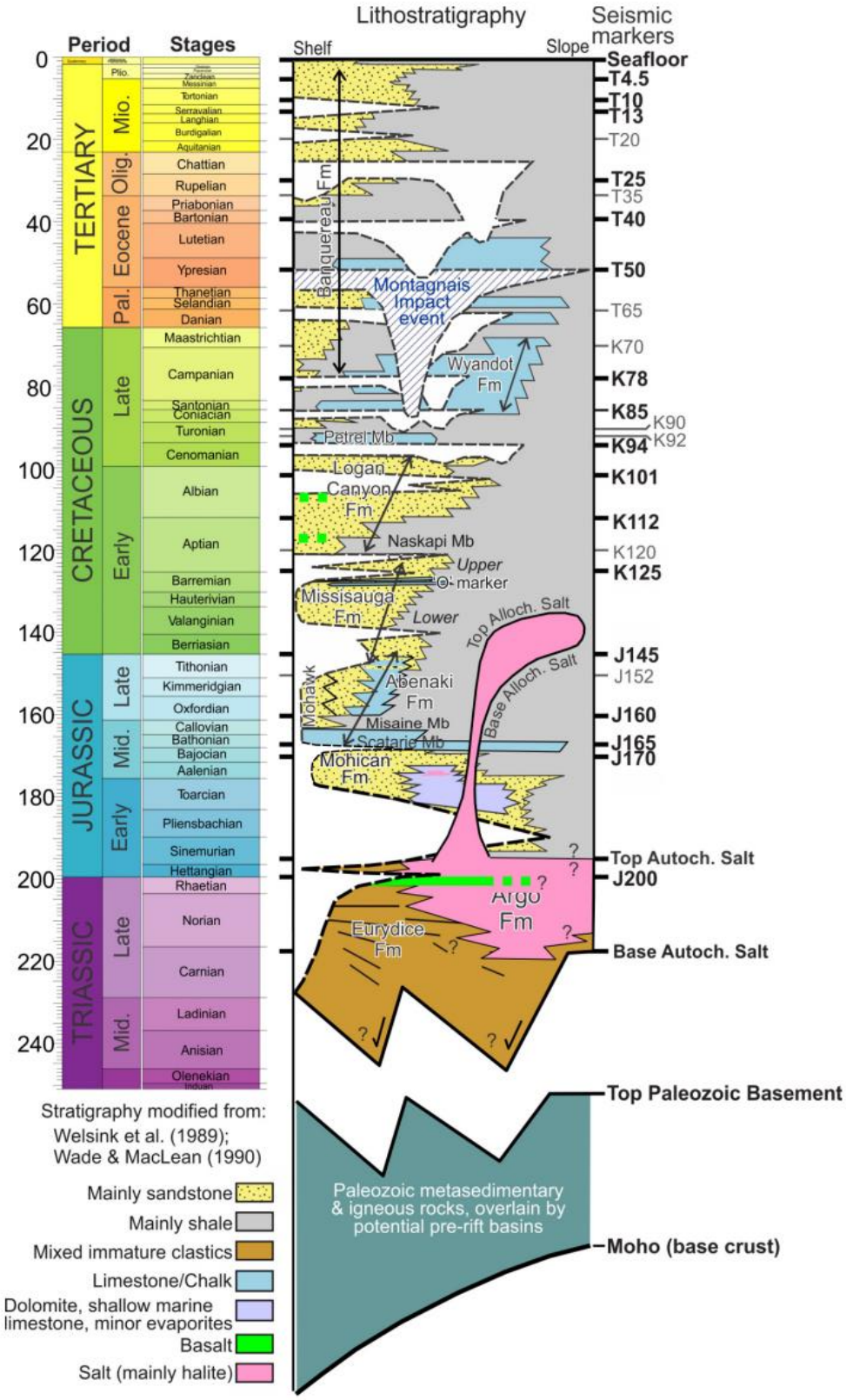

Figure 1.4. Overall stratigraphic column for the Scotian margin. (Deptuck and Kendell, 2020).

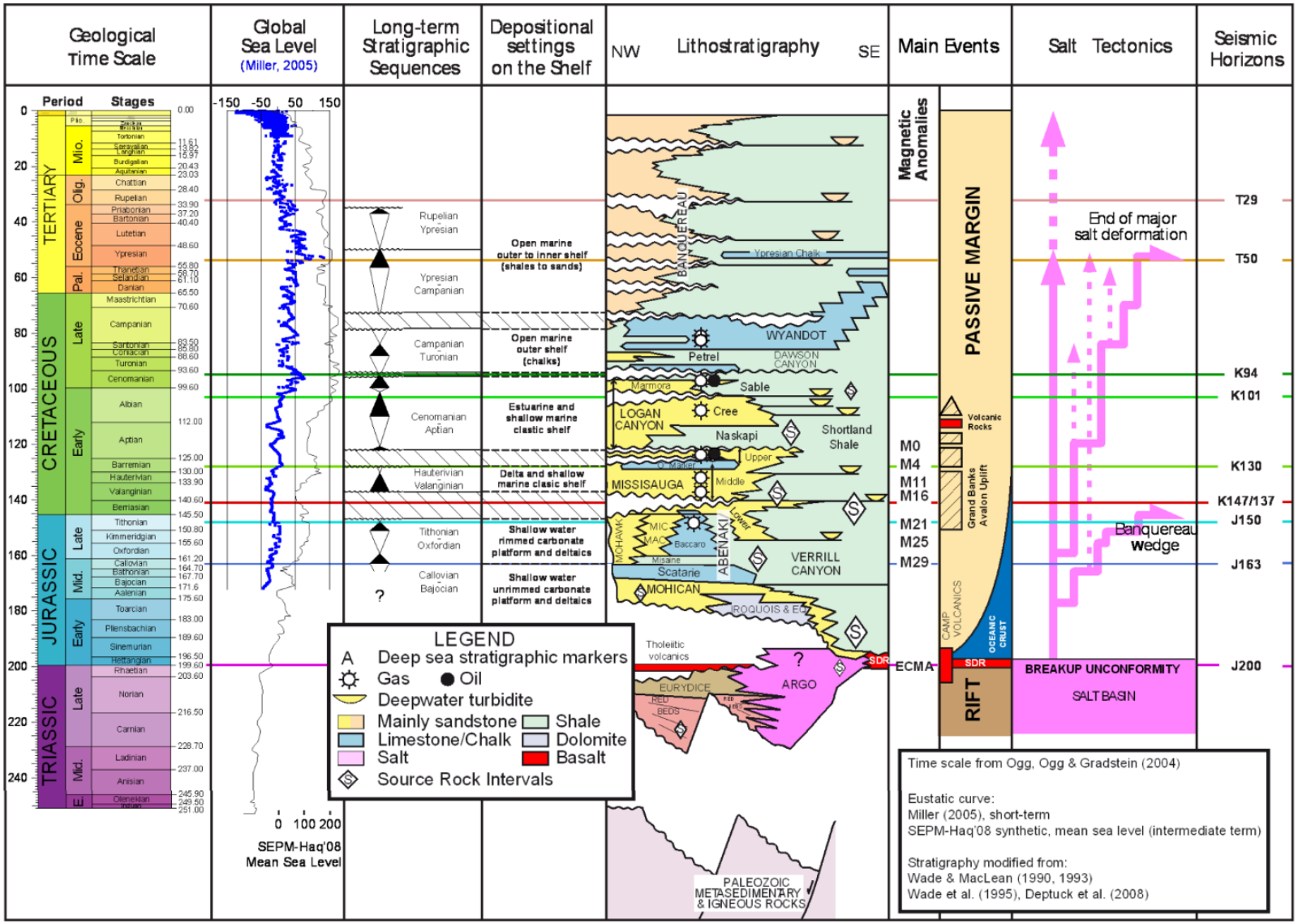

Figure 1.5. Updated stratigraphic chart of the Scotian Basin (Offshore Energy Technical Research Association, 2011).

1.4. Lithostratigraphy of the study interval

During the latest Jurassic, a rejuvenated plate separation between the Grand Banks and Iberia occurred, producing the Avalon Uplift east of the Scotian Basin (Fig. 1.2). Significant uplift, deformation, and extensive erosion of Jurassic and older strata occurred on the margin south of Newfoundland, causing a breakup unconformity known as the Avalon Unconformity (Offshore Energy Technical Research Association, 2011). Upper Jurassic to Lower Cretaceous strata includes the dominantly sandstone Missisauga Formation which represents a seaward prograding delta complex (Jansa and Wade, 1975), and laterally grades into the basinal mudrock Verrill Canyon Formation.

1.4.1. Missisauga Formation

The Missisauga Formation (Figs. 1.4, 1.5) is predominantly composed of sandstone beds separated by thin layers of argillaceous, medium light to brownish grey siltstone containing fine coalified plant fragments (McIver, 1972). The brownish grey to medium grey mudrock interbeds contain plant fragments, pyrite, and occasional siderite nodules. The sandstones are medium- to fine-grained and poorly to moderately sorted in the lower part of the formation (Figs. 1.6, 1.7). The upper portion of the formation yields coarse-grained sandstone with conglomerate beds at the base (Jansa and Wade, 1975). Throughout the formation, the sandstones are slightly argillaceous, range from moderately indurated to friable, and have good porosity.

The lower member of the Missisauga Formation consists of fine-grained to pebbly, often coarsening upward sandstone beds and minor thin limestone beds within a section of grey marine mudrock (Given, 1977). Deposition occurred in a delta front, possibly including barrier bar, beach and tidal channel deposits that grade upward into prodelta facies. Sediments of the Sable Island Delta were transported by local distributary systems to the terminal depositional areas of the fluvial delta (Wade and MacLean, 1990b). The lower member is overlain by the middle

member, which is characterized by coarse-grained sandstones. The upper member of the formation consists of coarse-grained (subangular to subrounded quartz grains), slightly argillaceous, and moderately indurated sandstones with conglomerate beds at the base (Jansa and Wade, 1975).

The Missisauga Formation is a seaward prograding delta complex with associated depositional systems, including alluvial plain, lower delta plain, and delta front. This is indicated by regional distribution, sedimentary composition, sedimentary structures (such as cross bedding, sharp contacts, scours, shale clasts, and graded sequences), lack of microfauna, and mechanical log characteristics (Jansa and Wade, 1975). Due to the fluvial-deltaic nature of deposits, the thickness of the Missisauga Formation is variable, ranging from absent to upwards of 2000 m in the Sable Sub-basin (Wade and MacLean, 1990b). The Missisauga Formation is limited at its base by a limestone unit at the top of the Kimmeridgian, or at the top of the Abenaki carbonates (Offshore Energy Technical Research Association, 2011) (Figs. 1.5, 1.6). The lower contacts with the underlying Mic Mac, Verrill Canyon, and Abenaki formations is conformable and gradational. The contact between the Missisauga Formation and overlying strata is conformable and sharp (Fig. 1.5; Jansa and Wade, 1975; Williams, 1975). Biostratigraphic studies (e.g., Barss et al., 1979) indicate that the age of the Missisauga Formation is Berriasian–Valanginian to Barremian, with the exception of uppermost Jurassic rocks occurring in the basal section of the formation in multiple wells.

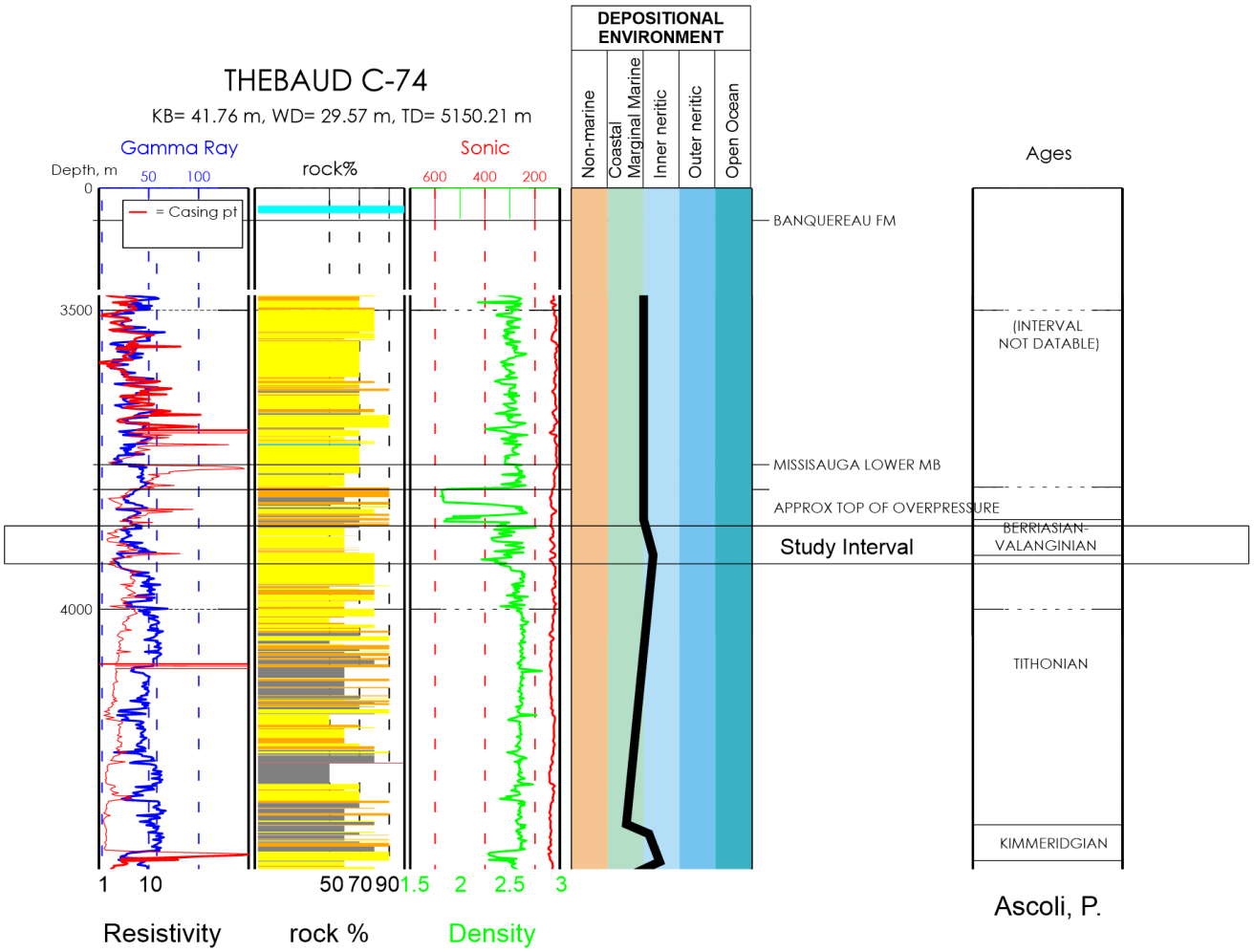

Figure 1.6. Updated lithology of the Thebaud C-74 well (Offshore Energy Technical Research Association, 2011).

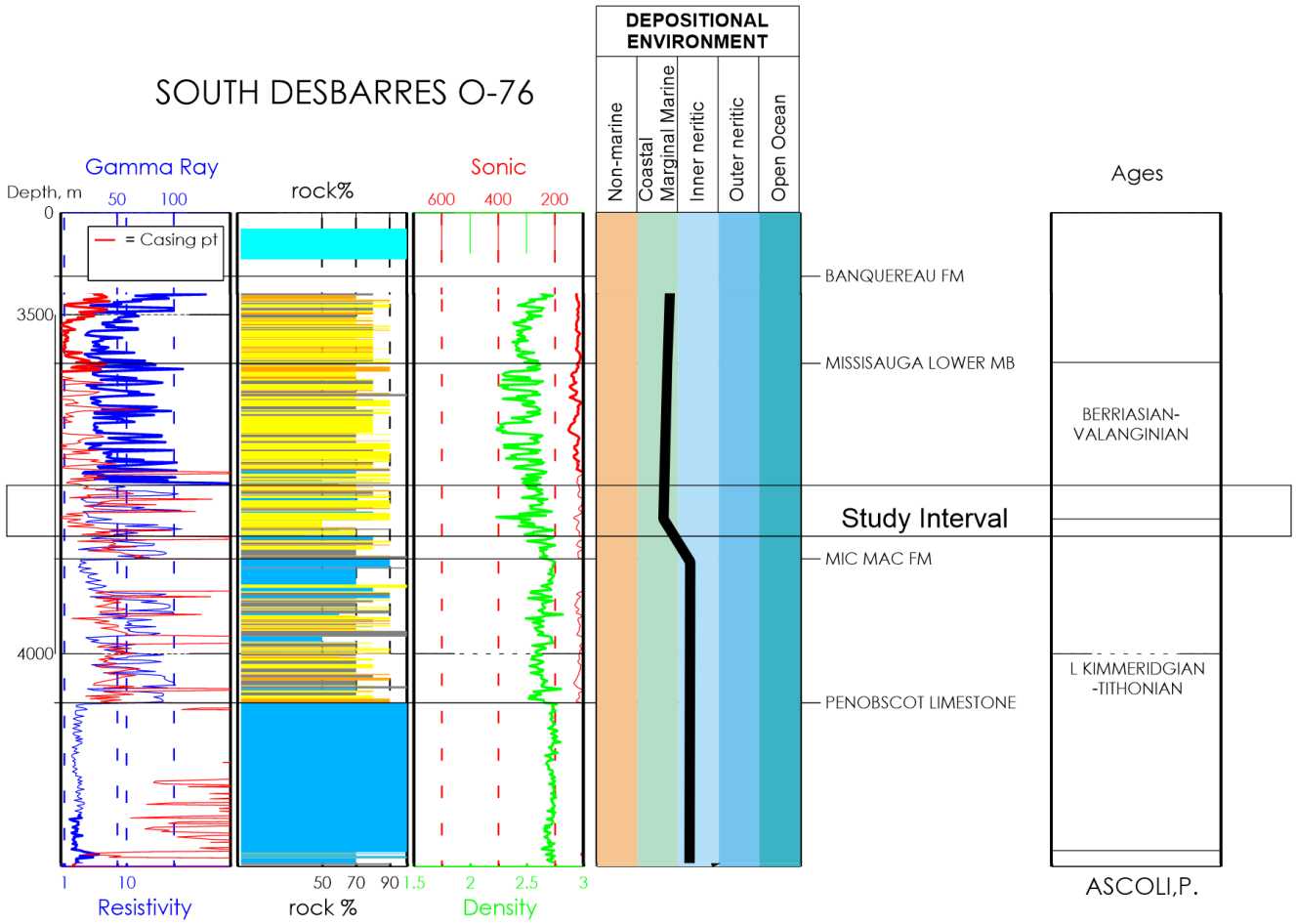

Figure 1.7. Updated lithology of the South Desbarres O-76 well (Offshore Energy Technical Research Association, 2011).

1.5. Biostratigraphy

The widely accepted biozonation for the Upper Jurassic to Lower Cretaceous strata on the Scotian Shelf (Table 1.1) was established using microfossils (mainly foraminifera but also ostracods and calpionellids), palynomorphs (predominantly dinoflagellate cysts (dinocysts) but also pollen, microspores and acritarchs), and nannofossils (primarily coccoliths) (Ascoli, 1976, 1981; Ascoli et al., 1984; Williams, 1975; Williams et al., 1990; Weston et al, 2012). The calcareous benthic foraminiferal zonation outlined by Ascoli (1976) (derived from Ohm (1967), Bartenstein (1976a, b, c), and Van Hinte (1976)) describes five biostratigraphic zones of the Late Jurassic. These approximately equate with the Bathonian, Callovian, Oxfordian, Kimmeridgian, and Tithonian.

Dinoflagellate zonations have been widely applied to the Jurassic rocks of the region by Williams (1975), Bujak and Williams (1978), and Davies (1985). Williams (1975) recognized four assemblage zones in the Middle to Late Jurassic of the Scotian Shelf: Bathonian–Callovian, Oxfordian, Kimmeridgian, and Tithonian. Palynomorphs are few to absent in the Oxfordian–Tithonian, likely due to unfavourable environmental conditions for dinoflagellate reproduction, or due to diagenetic processes that may have destroyed the cysts (Williams, 1975). There were also limited spores or pollen present.

Although Lower Cretaceous rocks are not distributed uniformly throughout the Scotian Shelf, Van Helden (1986) recognized two distinct dinocyst zones in the Berriasian–Valanginian of the basin. Ascoli (1976) designated a foraminiferal-ostracode zonation for the Scotian Basin based on the zonation proposed by Bolli (1966) and others. This was later updated by Williams et al. (1990) to include a zonation by Caron (1985). Williams (1975) described the Valanginian–Berriasian palynomorph zone as *Phoberocysta neocomica* within the Missisauga Formation, characterized by dinoflagellates *Achomosphaera neptuni* and *Phoberocysta neocomica* and the

first appearance of spores *Appendicisporites problematicus, Camarozonosporites insignis,* and *Trilobosporites apiverrucatus*. In the Valanginian, spores dominated the palynomorph assemblage, indicating a subtropical to tropical, flat and swampy lowland environment (Williams, 1975).

Ascoli (2004) completed a biostratigraphic study of microfossil assemblages (foraminifera and ostracoda) on the Thebaud C-74 washed cutting samples from 870 m to 5150 m. This study placed strata from 3850 m to 3890 m in the Berriasian–Valanginian, indicated by foraminifera such as *Lenticulina busnardoi, Lenticulina guttata, lenticulina sp., Epistomina tenuicostata,* and *Epistomina sp* (Ascoli, 2004). Tithonian-aged strata from 3910 m to 4340 m were identified by foraminifera such as *Epistomina stellicostata, Epistomina gr. Parastelligera-ventriosa, Lenticulina sp.,* and *Eoguttulina sp.,* and the ostracod *Cytherella sp.* Microfauna in this range were reported to be very scarce, with several barren samples identified. Strata from 3890 m to 3910 m were not assigned an age and are therefore represented as the suspected boundary within Thebaud C-74 cores 4 through 6 (Ascoli, 2004).

Weston et al., (2012) recently revised the biostratigraphic framework of the Scotian margin using core and cutting samples from select wells, including South Desbarres O-76, in which new nannofossil preparations and analyses were completed from the Kimmeridgian to the Valanginian. The studied micropaleontology and nannofossils of cores 1 and 2 were identified to be Late Tithonian in age. The suspected J/K boundary was placed at 3770 m based on micropaleontological evidence and wireline-log-lithological criteria identifying the Near Base Cretaceous Unconformity (NBCU), an unconformity that is typically recognized in the Verrill Canyon Formation, or the Middle or Lower members of the Missisauga Formation, as a biostratigraphic hiatus between the overlying Valanginian and underlying Berriasian or Tithonian strata (Weston et al., 2012). Upper Tithonian to Berriasian strata were barren of

nannofossils and had low-abundance and low-diversity nannofloras used as diagnostic taxa, such as *Watznaueria barnesae, Cyclagelosphaera margerelii,* and *Watznaueria britannica*. The dinocyst assemblages included *Cribroperidinium, Sentusidinium, Lanterna, Dichadogonyaulax pannea, Glossodinium dimorphum,* and *Senoniasphaera jurassica* (Weston et al., 2012). Barremian to Valanginian strata had low to moderate nannofossils, with some barren intervals. The nannofossil assemblages were predominantly comprised of *Watznaueria barnesae, Nannoconus,* and *Micrantholithus*. Also included were *Biscutum ellipticum, Conusphaera rothii, Diazomatolithus lehmanii, Micrantholithus hoschulzii, Micrantholithus obtusus, Nannoconus steinmannii,* and *Zeugrhabdotus erectus* (Weston et al., 2012). Preservation of these assemblages indicate that Upper Jurassic to Lower Cretaceous strata occur in the Scotian margin, and that the Jurassic–Cretaceous boundary is likely to be present within both studied wells.

Table 1.1. Diagnostic species of the Jurassic and Cretaceous palynomorph assemblage zones, Scotian Shelf and western Grand Banks (modified from Williams (1975)).

Age	Palynomorph Zone	Diagnostic Dinoflagellates	Diagnostic Spores and Pollen
Barremian	*Tenua anaphrissa* (peak)	*Cordosphaeridium fasciatum* *Meiourogonyaulax stoveri* *Muderongia simplex* *Muderongia tomaszowensis* *Oligosphaeridium asterigerum* *Polystephanephorus sarjeantii* *Pseudoceratium pelliferum* *Tenua anaphrissa*	*Cicatricosisporites brevilaesuratus*
Hauterivian	*Ctenidodinium elegantulum*	*Broomea jaegeri* *Callaiosphaeridium asymmetricum* (base) *Ctenidodinium elegantulum*	*Appendicisporites problematicus* *Cicatricosisporites hallei* *Contignisporites cooksonii*

		Gonyaulacysta serrata *Pseudoceratium pelliferum* (peak) *Systematophora complicata* *Wanaea limbriata*	*Matonisporites phlebopteroides*
Valanginian-Berriasian	*Phoberocysta neocomica* *Biorbifera johnewingi*	*Achomosphaera neptuni* *Phoberocysta neocomica* *Biorbifera johnewingi*	*Appendicisporites problematicus* (base) *Camarozonosporites insignis* (base) *Trilobosporites apiverrucatus* (base)
Tithonian	*Ctenidodinium panneum*	*Ctenidodinium culmulum* *Ctenidodinium panneum* *Lanterna sportula* *Pyxidiella sp.*	*Inaperturopollenites sp.*
Kimmeridgian	*Gonyaulacysta cladophora*	*Epiplosphaera bireticulata* *Gonyaulacysta cladophora* *Hexagonifera jurassica* *Imbatodinium villosum* *Scriniodinium crystallinum* *Systematophora fasciculigera* *Taeniophora iunctispina*	*Cicatricosisporites australiensis* (base) *Classopollis classoides* *Coronatispora valdensis* (base) *Exesipollenites tumulus*
Oxfordian	*Gonyaulacysta jurassica*	*Adnatosphaeridium aculleryi* *Ctenidodinium ornatum* *Gonyaulacysta jurassica* *Leptodinium egemenii* *Systematophora areolata*	*Callialasporites dampieri* (base) *Contignisporites cooksonii* (base) *Leptolepidites psarosus* (base)
Middle Jurassic	*Valensiella vermiculata*	*Meiourogonyaulax sp.* *Valensiella ovulum* *Valensiella vermiculata*	*Classopollis classoides*

CHAPTER 2

METHODOLOGY

2.1. Sampling

Sub-samples of the Missisauga formation preserved in conventional cores at Thebaud C-74 and South Desbarres O-76 were taken at 1 m to ~30 cm intervals. Higher resolution sampling was conducted in uppermost Tithonian to lowermost Berriasian strata preserved in the conventional cores to capture the Jurassic–Cretaceous boundary. Samples were taken from cores 1 through 6 in the Thebaud C-74 well and cores 1 and 2 in the South Desbarres O-76 well and cuttings were sub-sampled to supplement the core material from the South Desbarres O-76 well every 5 m from 3750–3800 m. Cuttings samples were washed to remove drilling muds and oils that can cause geochemical contamination. All samples were crushed and powdered using an agate mortar.

2.2. Total Organic Carbon, Total Organic Nitrogen, $\delta^{13}C_{org}$, and $\delta^{15}N_{air}$

Total Organic Carbon, TON, $\delta^{13}C_{org,}$ and $\delta^{15}N_{air}$ were measured using the analytical protocol outlined by Kikumoto et al. (2014). All measurements were conducted at the isotope lab of Memorial University of Newfoundland (MUN) using a Delva V Plus Isotope Ratio Mass Spectrometer equipped with a conventional elemental analyzer and an interfaced OI Analytical Aurora 1030W TOC analyzer. About 0.5 g of sample powder was placed in 50 mL centrifuge plastic vials and digested in HCl following protocol outlined by Vindušková et al. (2019). Up to 150 mg of each digested sample was combusted at 1000°C using a Carlos Erba elemental analyzer coupled with a Thermofinnigan DELTA V plus IRMS through a Conflow interface. The $\delta^{13}C_{org}$ calibration was done using standards G-91 (low organic soil) ($\delta^{13}C_{org}$ (VPDB) = -26.71 ± 0.24) and high organic sediment B2151 ($\delta^{13}C_{org}$ (VPDB) = -28.90 ± 0.10). TOC calibration was

done using standards D-Fructose ($\delta^{13}C_{org}$ (VPDB) = -10.53 ± 0.11, %C = 40.00), MUN-CO-2 ($\delta^{13}C_{org}$ (VPDB) = -40.11 ± 0.15), and acetanlide ($\delta^{13}C_{org}$ (VPDB) = -27.14 ± 0.20, %C = 71.09). The standards used for $\delta^{15}N_{air}$ were B2151 high-organic sediment ($\delta^{15}N_{air}$ = 4.35 ± 0.20‰ air), L-Glutamic Acid ($\delta^{15}N_{air}$ = -2.77 ± 0.18 ‰), and acetanlide ($\delta^{15}N_{air}$ = 0.63 ± 0.15 ‰). The standards used for TON calibration were IAEA-N2 ($(NH_4)_2SO_4$) ($\delta^{15}N_{air}$ = 20.32 ± 0.09 ‰), USGS-25 ($(NH_4)_2SO_4$) ($\delta^{15}N_{air}$ = -30.25 ± 0.38).

2.3. Elemental Analysis

Bulk elemental analysis was determined following the methodology outlined by Kendall et al. (2010). The powder samples (50 mg each in a PFA beaker) were dissolved completely in a mix of concentrated HF-HNO_3, put on a hot plate for 24h at 100°C, and left to evaporate until dry. The residues were dissolved in 5 mL HCl 6N and kept as archive solutions. Trace elements were measured on a HR-ICP-MS Thermofisher Scientific Element XR at PSO (Pôle de Spectrométrie Océan, IUEM, Brest, France). An aliquot of archive solution was diluted in 2.5% HNO_3 doped with indium as an internal standard for correction of signal drift during measurements. Sample concentrations were calibrated using in-house external calibration standards. Two standards BHOV2 and CAL-S were prepared and run with the samples as well as procedural blanks. The samples were ashed at 550°C for 24 hours in a muffle furnace to oxidize organic matter and were cooled and transferred to 22 mL Savillex Teflon beakers where they were digested with multiple combinations of concentrated trace-metal grade acids at 110°C. The samples were digested using 2.5 mL HNO_3 and 0.5 mL HF for 48 hours, followed by a second digestion using 1 mL HNO_3 and 3 mL HCl for 48 hours, and finally a third digestion using 2 mL HCl for 24 hours. A stock solution containing 5 mL of 6M HCl and three drops of 0.5% HF was prepared and stored in 15 mL low density polyethylene (LDPE) vials. After dissolution, sample splits were dried, diluted with 2% HNO_3 and analyzed for major, minor, and trace element

abundances using Inductively Coupled Plasma Mass Spectrometry (ICP-MS). Uncertainty of analyses was better than 5%.

2.4. Enrichment Factors

Enrichment factors (EFs) of U, Mo, Ni, V, Cr, Mn, Zn, and Cu were calculated using the following equation, using Al as the reference element and Post-Archean-Australian Shale (PAAS) as the standard:

$$EF_{PAAS} = (\text{trace metal/Al})_{sample} / (\text{trace metal/Al})_{PAAS}$$

(Taylor and McLennan, 1985; Calvert and Pederson, 1993; Tribovillard et al., 2006; Tribovillard et al., 2012). Iron and P were converted into enrichment factors through normalization to the Upper Crust values using the formula:

$$EF_{\text{Upper Crust}} = (\text{trace metal/Al})_{sample} / (\text{trace metal/Al})_{\text{Upper Crust}}$$

(McLennan, 2001). The EF values >1 are generally considered to be enrichment relative to PAAS or Upper Crust, while values <1 are considered to be depletions (Tribovillard et al., 2006).

CHAPTER 3

RESULTS

The geochemical results are shown in Appendix A and their statistics are summarized in Table 3.1. The geochemical profiles of the enrichment factors across the investigated intervals are shown in Figures 3.1 and 3.2. Profiles of paleoredox (TOC, TON, U, Mo, V, Cr, Fe, Mn, and Th/U), productivity ($\delta^{13}C_{org}$, $\delta^{15}N_{air}$, TOC, TON, Ni, Cu, P, and Zn), terrigenous input (Al, Ti, Al/Ti, K/Al, and ∑REE), and paleosalinity (B/Ga) display a consistent anomaly in successions preserved in both the Thebaud C-74 (3909.19 m to 3916.2 m) and South Desbarres O-76 (3806.53 m to 3815.39 m) wells (Figs. 3.1 and 3.2).

The upper and lower parameters of the geochemical anomaly are set to encompass distinct shifts, either positive or negative, that occur across all the proxies at the same horizon. Table 3.2 summarizes the R^2 values representing the correlation between TOC/TON and elemental concentrations and EFs for the total well and geochemical anomaly intervals of both wells.

Table 3.1. Summary statistics of isotopic and trace element geochemical compositions of the shales and sandstones of the investigated Thebaud C-74 and South Desbarres O-76 wells.

Thebaud C-74 Total Well										
Total	U (ppm)	V (ppm)	Mo (ppm)	Cr (ppm)	Fe (ppm)	Mn (ppm)	Al (ppm)	Ti (ppm)	∑REE	K/Al
n	38	38	38	38	38	38	38	38	38	38
Mean	2.1	97	2.0	102	43825	400	142637	6592	230	0.2
Stdev	1.3	60	1.9	42	25764	361	168691	3663	188	0.1
Max	5.0	219	8.5	194	136206	1935	577966	14143	835	0.3
Min	0.4	21	0.3	21	9904	40	11771	771	40	0.1

Thebaud C-74 Total Well										
Total	Ni (ppm)	Cu (ppm)	P (ppm)	Zn (ppm)	$\delta^{13}C_{org}$	TOC	$\delta^{15}N_{air}$	TON	Th/U	B/Ga
n	38	38	38	38	73	73	73	73	38	38
Mean	44	18	560	177	-25.9	1.1	4.0	0.1	4.4	3.8
Stdev	39	39	278	322	0.4	1.1	10	0.1	0.7	1.1
Max	235	50	1193	1940	-25.1	4.7	19	0.5	6.3	6.6
Min	4.6	1.8	141	17	-26.9	0.0	-23	0.0	2.8	0.6

Thebaud C-74 Geochemical Anomaly										
Total	U (ppm)	V (ppm)	Mo (ppm)	Cr (ppm)	Fe (ppm)	Mn (ppm)	Al (ppm)	Ti (ppm)	∑REE	K/Al
n	6	6	6	6	6	6	6	6	6	6
Mean	1.7	78	2.8	97	52800	312	120878	5302	200	0.1
Stdev	1.4	75	3.2	54	45360	204	224421	4634	289	0.1
Max	4.1	219	7.9	194	136206	571	577966	14143	835	0.2
Min	0.4	21	0.4	34	17316	40	12855	1587	40	0.1

Thebaud C-74 Geochemical Anomaly										
Total	Ni (ppm)	Cu (ppm)	P (ppm)	Zn (ppm)	$\delta^{13}C_{org}$	TOC	$\delta^{15}N_{air}$	TON	Th/U	B/Ga
n	6	6	6	6	10	10	10	10	6	5
Mean	64	18	339	375	-25.9	1.1	6.5	0.1	4.1	3.1
Stdev	87	18	182	767	0.4	1.5	3.8	0.2	0.8	2.2
Max	235	50	685	1940	-25.3	4.7	13	0.4	5.1	6.6
Min	9.9	2.7	195	28	-26.5	0.1	-0.8	0.0	2.8	0.6

South Desbarres O-76 Total Well										
Total	U (ppm)	V (ppm)	Mo (ppm)	Cr (ppm)	Fe (ppm)	Mn (ppm)	Al (ppm)	Ti (ppm)	∑REE	K/Al
n	22	22	22	22	22	22	22	22	22	22
Mean	2.8	126	2.1	155	44971	351	100346	8560	231	0.3
Stdev	1.7	69	1.3	87	19780	226	99673	5703	149	0.1
Max	8.2	284	5.1	368	86493	840	425408	25591	645	0.4
Min	0.3	16	0.1	20	7765	71	14426	675	42	0.1

South Desbarres O-76 Total Well										
Total	Ni (ppm)	Cu (ppm)	P (ppm)	Zn (ppm)	$\delta^{13}C_{org}$	TOC	$\delta^{15}N_{air}$	TON	Th/U	B/Ga
n	22	22	22	22	36	36	36	36	22	22
Mean	73	21	787	98	-25.9	2.1	6.4	0.2	3.6	4.4
Stdev	46	9.8	380	94	0.4	2.1	4.3	0.1	0.6	1.0
Max	174	39	2034	448	-25.1	8.3	11	0.5	5.1	5.8
Min	6.6	2.9	110	21	-26.8	0.1	-6.2	0.0	2.8	1.8

South Desbarres O-76 Geochemical Anomaly										
Total	U (ppm)	V (ppm)	Mo (ppm)	Cr (ppm)	Fe (ppm)	Mn (ppm)	Al (ppm)	Ti (ppm)	∑REE	K/Al
n	6	6	6	6	6	6	6	6	6	6
Mean	4.0	179	3.0	235	66738	268	184805	12509	349	0.2
Stdev	1.2	54	1.1	65	15849	81	157562	4572	98	0.1
Max	6.0	227	5.1	328	86493	378	425408	20701	493	0.3
Min	2.9	91	2.1	177	51688	196	24581	8210	206	0.1

South Desbarres O-76 Geochemical Anomaly										
Total	Ni (ppm)	Cu (ppm)	P (ppm)	Zn (ppm)	$\delta^{13}C_{org}$	TOC	$\delta^{15}N_{air}$	TON	Th/U	B/Ga
n	6	6	6	6	13	13	13	13	6	6
Mean	122	30	949	127	-25.9	2.7	5.2	0.3	3.9	4.4
Stdev	45	6.1	216	73	0.4	2.1	4.3	0.1	0.4	1.2
Max	174	39	1203	250	-25.5	7.3	10	0.4	4.5	5.3
Min	69	69	617	64	-26.8	0.1	-5.0	0.1	3.6	2.2

Table 3.2. R^2 value between TOC/TON and redox (U, V, Mo) and productivity (P, Ni, Cu, Zn) proxies for the total well and geochemical anomaly intervals of both wells.

TOC/TON vs TEs (ppm) for Total Well								
		U (ppm)	V (ppm)	Mo (ppm)	P (ppm)	Ni (ppm)	Cu (ppm)	Zn (ppm)
Thebaud C-74	TOC	0.1	0.1	0.4	0.1	0.5	0.2	0.01
	TON	0.6	0.7	0.3	0.4	0.6	0.8	0.00009
South Desbarres O-76	TOC	0.2	0.4	0.3	0.1	0.5	0.3	0.1
	TON	0.3	0.7	0.5	0.4	0.5	0.6	0.3

TOC/TON vs TEs (ppm) for Geochemical Anomaly								
		U (ppm)	V (ppm)	Mo (ppm)	P (ppm)	Ni (ppm)	Cu (ppm)	Zn (ppm)
Thebaud C-74	TOC	0.1	0.02	0.4	0.1	0.8	0.6	0.1
	TON	0.7	0.6	0.2	0.6	0.7	0.7	0.2
South Desbarres O-76	TOC	0.8	0.4	0.9	0.0000001	0.2	0.6	0.3
	TON	0.02	0.6	0.2	0.2	0.00001	0.2	0.02

TOC/TON vs TEs (EF) for Total Well								
		U (EF_{PAAS})	V (EF_{PAAS})	Mo (EF_{PAAS})	P ($EF_{UpperCrust}$)	Ni (EF_{PAAS})	Cu (EF_{PAAS})	Zn (EF_{PAAS})
Thebaud C-74	TOC	0.04	0.04	0.02	0.1	0.2	0.05	0.02
	TON	0.1	0.2	0.01	0.6	0.03	0.0002	0.05
South Desbarres O-76	TOC	0.0004	0.02	0.00003	0.03	0.01	0.004	0.02
	TON	0.1	0.03	0.04	0.2	0.01	0.05	0.02

TOC/TON vs TEs (EF) for Geochemical Anomaly								
		U (EF_{PAAS})	V (EF_{PAAS})	Mo (EF_{PAAS})	P ($EF_{UpperCrust}$)	Ni (EF_{PAAS})	Cu (EF_{PAAS})	Zn (EF_{PAAS})
Thebaud C-74	TOC	0.2	0.1	0.0003	0.02	0.7	0.1	0.1
	TON	0.1	0.1	0.03	0.2	0.01	0.05	0.02
South Desbarres O-76	TOC	0.001	0.0002	0.002	0.1	0.05	0.04	0.03
	TON	0.7	0.6	0.6	0.7	0.6	0.7	0.6

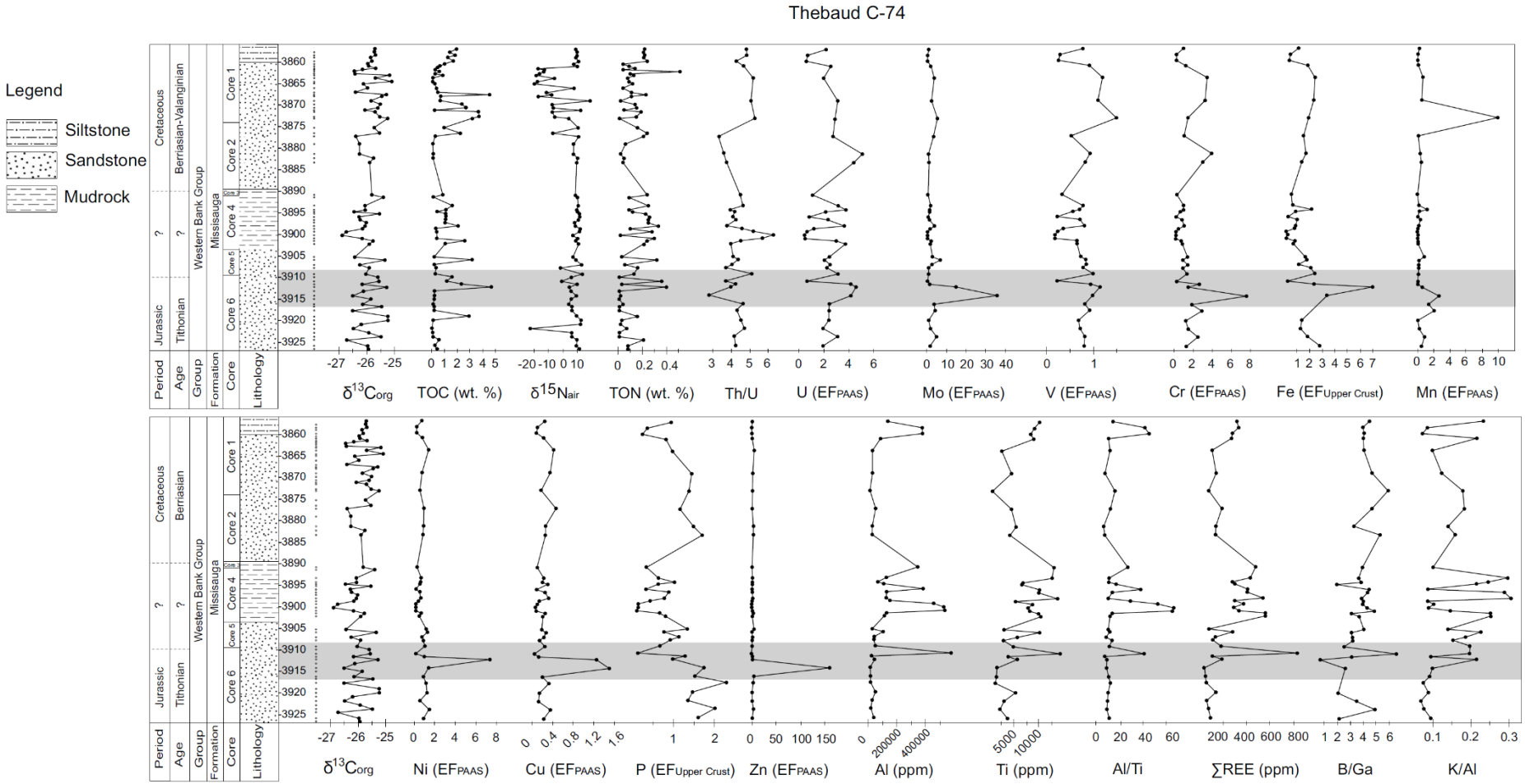

Figure 3.1. The profiles of $\delta^{13}C_{org}$, TOC, Th/U, U (EF_{PAAS}), Mo (EF_{PAAS}), V (EF_{PAAS}), Cr (EF_{PAAS}), Fe ($EF_{Upper\ Crust}$), Mn (EF_{PAAS}), $\delta^{15}N_{air}$, TON, Ni (EF_{PAAS}), Cu (EF_{PAAS}), P ($EF_{Upper\ Crust}$), Zn (EF_{PAAS}), Al, Ti, Al/Ti, K/Al, and ∑REE of the Thebaud C-74 well. The black dots mark the stratigraphic levels of the collected samples. Grey shading represents the geochemical anomaly. Stratigraphic boundaries based on biostratigraphy from Ascoli (2004). Lithology based on Mumcuoglu et al., 1986.

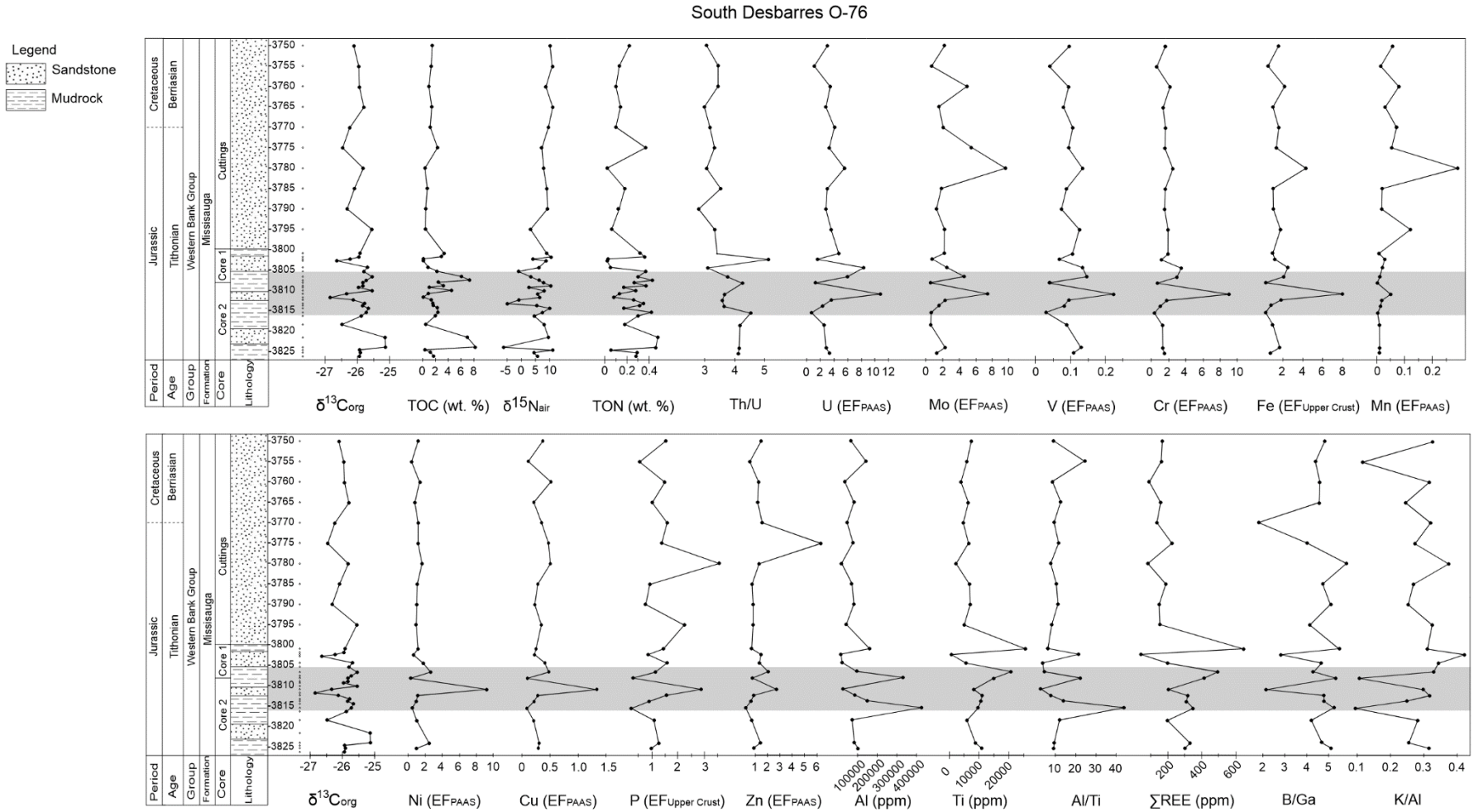

Figure 3.2. The profiles of $\delta^{13}C_{org}$, TOC (wt. %), Th/U, U (EF_{PAAS}), Mo (EF_{PAAS}), V (EF_{PAAS}), Cr (EF_{PAAS}), Fe ($EF_{Upper\ Crust}$), Mn (EF_{PAAS}), $\delta^{15}N_{air}$, TON (wt.%), Ni (EF_{PAAS}), Cu (EF_{PAAS}), P ($EF_{Upper\ Crust}$), Zn (EF_{PAAS}), Al, Ti, Al/Ti, K/Al, and ∑REE of the South Desbarres O-76 well. The black dots mark the stratigraphic levels of the collected samples. Grey shading represents geochemical anomaly. Stratigraphic boundaries based on biostratigraphy from Weston et al., 2012. Lithology based on Sine et al., 1984.

3.1. Paleoredox proxies (TOC, TON, U, Mo, V, Cr, Fe, Mn, Th/U)

Thebaud C-74

The paleoredox proxies increase between 3911.57 m and 3914.22 m in Thebaud C-74. The EF profiles of U, Mo, V, Cr, Fe, and Mn increase above 1 at this depth, demonstrating enrichment (Fig. 3.1). The U, V, Mo, Cr, Fe, and Mn profiles experience a positive excursion from 3911.57 m to 3914.22 m with the peak of U, V, and Fe occurring at 3912.24 m, and the peak of Mo, Cr, and Mn occurring at 3914.22 m. Conversely, the Th/U ratio exhibits a negative excursion, with minimum values at 3914.22 m. The TOC and TON both experience positive excursions that peak at 3912.24 m, paralleling the peak in the U, V, and Fe profiles.

South Desbarres O-76

In the South Desbarres O-76 well, the profiles of the redox sensitive elements and their ratios show excursions between 3806.53 m to 3815.39 m (Fig. 3.2). A positive excursion of ~8 in the profiles of U, V, Mo, Cr, Fe, and Mn occurs starting at 3815.39 m, and peaking at 3810.82 m. The TOC profile shows a correlated negative excursion (up to 6%; Fig. 3.2) The Th/U ratio exhibits a similar trend to Thebaud C-74, with a negative excursion peaking at 3.5 between 3813.70 m and 3810.82 m.

3.2. Productivity proxies ($\delta^{13}C_{org}$, $\delta^{15}N_{air}$, TOC, TON, Ni, Cu, P, Zn)

Thebaud C-74

The $\delta^{13}C_{org}$ profile exhibits a negative excursion of ~1.5‰ at 3914.22 m that correlates with a negative $\delta^{15}N_{air}$ (to 4.6 ‰), positive TOC (to 4.65 %) and TON (poor, ~0.5%) shifts (Fig. 3.1). The Ni, Cu, and Zn profiles all exhibit a pronounced positive shift from 3914.22 m to 3912.24 m that almost mirrors the negative $\delta^{13}C_{org}$ excursion. The P ($EF_{Upper\ Crust}$) values fluctuate throughout this interval, trending downward throughout the anomaly.

South Desbarres O-76

The $\delta^{13}C_{org}$ profile exhibits a negative excursion of ~2.5‰ at 3811.70 m (Fig. 3.2). The TOC values are 2.3% at 3814.38 m and decrease to 0.09% upcore at 3811.70 m. They exhibit an almost parallel negative excursion correlated with the $\delta^{13}C_{org}$ excursion. The $\delta^{15}N_{air}$ curve shows a general positive excursion of ~15‰ that starts at 3814.38 m, whereas the TON profile shows a small negative shift (~0.3%) and both almost correlate with the negative $\delta^{13}C_{org}$. The Ni, Cu, P, and Zn profiles all exhibit pronounced positive excursions (at 3810.82 m) that are correlated with those shown by the $\delta^{13}C_{org}$, TOC, TON, and $\delta^{15}N_{air}$ profiles. Trace element concentrations (Table 3.1) are generally higher in this well than those of the Thebaud C-74 well, except for the Zn values.

The negative $\delta^{13}C_{org}$ shifts of both studied cores can be globally correlated with similar δ13Corg excursions recorded by equivalent successions in other locations and on different paleocontinents (Galloway et al., 2020; Price et al., 2016; Barragan et al., 2020; Martínez-Yáñez et al. 2017; Michalik et al., 1995; Grabowski et al., 2010; Föllmi, 2012; Capelli et al., 2020).

3.3. Terrigenous input proxies (Al, Ti, Al/Ti, K/Al, ∑REE)

In Thebaud C-74, a pronounced positive shift in the Al, Ti, Al/Ti, K/Al, and ∑REE profiles occurs between 3910.87 m and 3909.19 m (Fig. 3.1). In South Desbarres O-76, the Al and Al/Ti trends exhibit two positive shifts; a maximum peak at 3815.39 m followed by another peak at 3808.08 m (Fig. 3.2). Titanium, K/Al, and ∑REE peak at 3806.53 m. The average Al values within Thebaud C-74 are higher than those of the South Desbarres O-76 well (142647 ppm and 100346 ppm, respectively), whereas the average Ti values of this well (6592 ppm) are lower than those of the South Desbarres O-76 well (8560 ppm).

3.4. Paleo-salinity (B/Ga)

In Thebaud C-74, the B/Ga profile shows an increase at 3910.87 m that is contemporaneous with a peak in the terrigenous input proxies. In South Desbarres O-76, the B/Ga ratio values are >4.7 from 3812.31 m to 3815.39 m. A negative excursion occurs at 3810.82 m, followed by a return to relatively high values (>4.3) by 3808.08 m.

CHAPTER 4

DISCUSSION

4.1. Geochemical Preservation

A consideration of the integrity of the geochemical record is necessary for a discussion of usage of elemental concentrations and their ratios as paleoenvironmental proxies in marine sediments. In siliciclastic sediments, progressive burial is associated with increased temperatures and water/rock interactions at depth. Above 50°C, diagenetic alteration results in the release of hydrocarbons, which leads to an overall decrease in TOC. This also causes an increase in $\delta^{13}C_{org}$ and $\delta^{15}N_{air}$ values due to the release of organic compounds that are ^{12}C- and ^{14}N-enriched (Faure and Mensing, 2004). Therefore, a significant correlation between $\delta^{13}C_{org}$ and TOC, and $\delta^{15}N_{air}$ and TOC can reflect the influence of diagenetic alteration on isotopic signatures. The organic carbon-isotope composition can also be affected by the type of OM, but no differentiation of organic matter source was herein conducted. The $\delta^{13}C_{org}$ values in both Thebaud C-74 and South Desbarres O-76 vary in their correlations with TOC between insignificant ($R^2 = 0.234$; $p = 0$) and moderate ($R^2 = 0.458$; $p = 0$; Fig. 4.1), respectively. The $\delta^{15}N_{air}$ and TOC are insignificantly correlated ($R^2 = 0.002$ Thebaud C-74, $R^2 = 0.052$ South Desbarres O-76; $p = 0$; Fig. 4.1). The lack of relationship suggests preservation of at least near-primary $\delta^{13}C_{org}$ and $\delta^{15}N_{air}$ signatures.

$R^2 = 0.234$

Thebaud C-74

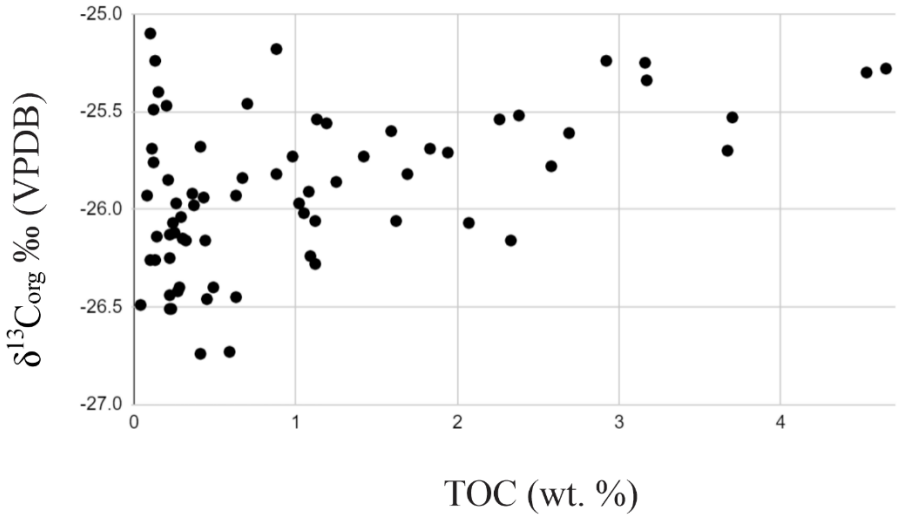

$R^2 = 0.002$

Thebaud C-74

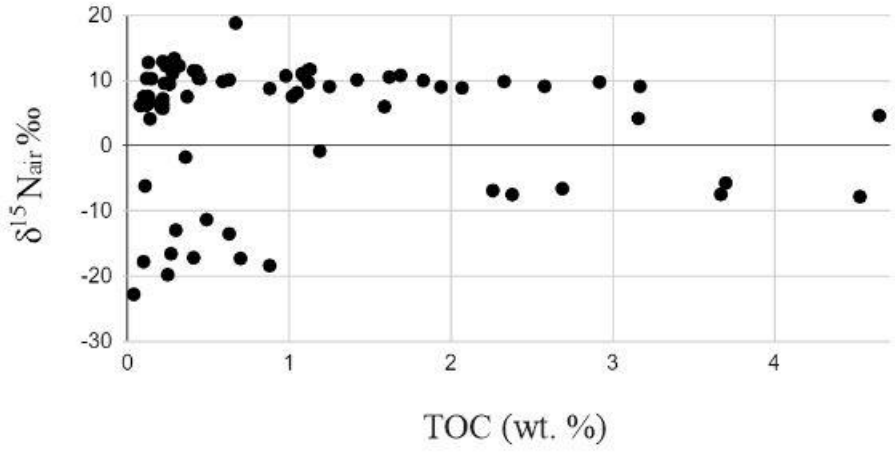

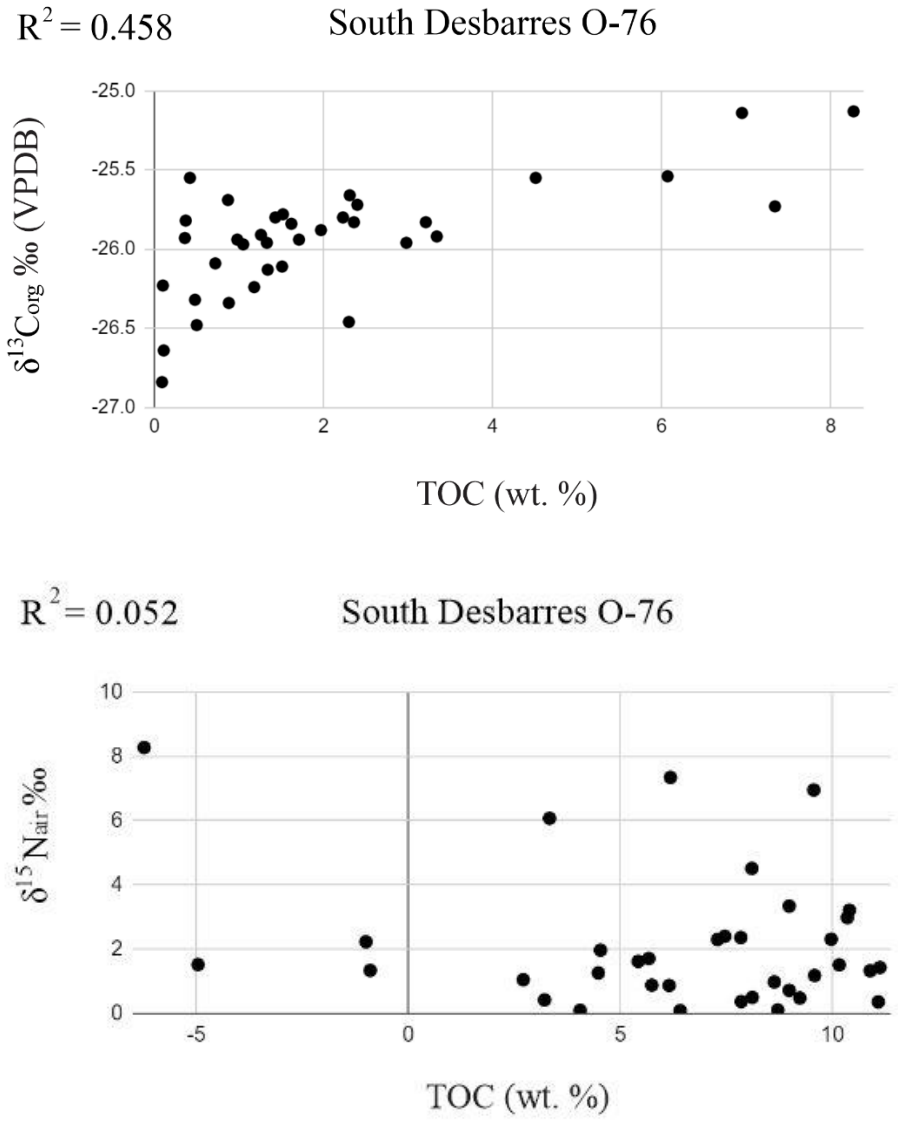

Figure 4.1. $\delta^{13}C_{org}$ vs TOC and $\delta^{15}N_{air}$ vs TOC for the Thebaud C-74 and South Desbarres O-76 wells.

4.2. Evaluation of TOC and TON

The amounts of TOC and TON reflect both OM accumulation and preservation (Canfield, 1994; Murphy et al., 2000; Shoepfer et al., 2014). The relationship between TOC/TON and elemental concentrations, ratios, and enrichment factors can potentially enable the identification of the proxies most closely related to the accumulation of organic carbon and

nitrogen, that are in turn related to productivity and increased preservation under low oxygen conditions (Hatch and Leventhal, 1992; Algeo and Maynard, 2004; Rimmer, 2004; Algeo and Lyons, 2006; Piper and Calvert, 2009; Tribovillard et al., 2012: Schoepfer et al., 2014). During periods of increased primary productivity, there are high abundances of photosynthetic microorganisms, which utilize micronutrients and take up ^{12}C. As these microorganisms die, they sink to the seafloor, transporting any trace elements bound to the OM. Higher abundances of TOC/TON (and thereby OM) reflect elevated levels of primary productivity. The buried OM can be preserved to varying degrees, depending on how much oxygen is in the sediment. Higher oxygen levels cause the OM to oxidize and decompose, potentially releasing any elements bound in the OM back into the water column, while anoxic settings prevent decomposition and preserve the OM.

No single proxy, or set of proxies, display a strong correlation ($R^2 > 0.5$) with TOC or TON (Table 3.2), which does not identify either reducing conditions or elevated productivity as the single driving factor for OM accumulated. This likely reflects development of both elevated productivity and low oxygen conditions that promoted preservation of OM in sediments.

4.3. Paleoredox proxies

The concentration of redox sensitive trace elements in marine sediments can be used to provide information about paleoredox conditions during deposition (e.g., Tribovillard et al., 2006; Śliwinski et al., 2010; Wignall et al., 2007; Wignall and Twitchett, 1996; Algeo and Maynard, 2004). Since individual redox sensitive trace elements have varying mechanisms for remobilization after deposition and burial, and inaccurate signals can be recorded due to accumulation from multiple origins, they are often evaluated using a multi-proxy approach to ensure that the analyzed trends are truly representative of the paleoenvironmental conditions

(Tribovillard et al., 2006). Paleoredox conditions for both wells (Figs. 3.1 and 3.2) are interpreted from the Th/U ratio and EFs of U, Mo, V, Cr, Fe, and Mn profiles. These profiles in Thebaud C-74 (Fig. 3.1) all exhibit a shift (geochemical anomaly) between 3909.19 m and 3916.20 m that reflects the development of more reducing conditions at the start of the anomaly, followed by a shift to more oxidizing conditions at the end of the anomaly. A similar trend is exhibited in the South Desbarres O-76 well (Fig. 3.2), where two distinct shifts to more reducing conditions are indicated between 3806.53 m and 3815.39 m (the geochemical anomaly) separated by a shift to a more oxygenated environment.

The geochemical anomaly within the Thebaud C-74 well is composed of six samples (Table 3.1; Fig. 3.1). The paleoredox profiles reconstructed from these samples suggest a shift to euxinic conditions at 3914.22 m to 3912.24 m (Appendix A; Table 3.1). This is indicated by the positive excursion in all the profiles, including Mo (EF_{PAAS}), which increases to a maximum of 36. Anoxia is further represented at this depth (3914.22 m to 3912.24 m) in Thebaud C-74 by a positive excursion in the profiles of U and V to 4.6 and 1.1, respectively, at 3912.24 m, and TOC values to 4.7 wt.% (Fig. 3.1). This suggests a lack of oxygen at, or just below, the sediment water interface that facilitated the preservation of organic matter (Canfield, 1994; Hatch and Leventhal, 1992; Piper and Calvert, 2009). Additionally, a low Th/U ratio (2.8) is observed at 3914.22 m (Fig. 3.1), further supporting a shift to anoxia from 3914.24 m to 3912.22 m. At 3910.87 m in Thebaud C-74, all paleoredox proxies exhibit a negative shift, indicating the development of more oxic conditions (Fig. 3.1). The profiles of Mo, Cr, Fe and Mn remain low, and the Th/U ratio is >2, throughout the rest of the anomaly and upwards in the well. Conversely, the U and V profiles experience a smaller subpeak at 3909.19 m to 3.1 and 1.0, indicating a reversion to anoxic/ferruginous (Fe reducing) conditions without the presence of free H_2S.

The geochemical anomaly within the South Desbarres O-76 well spans six samples from 3815.39 m to 3806.53 m. (Table 3.2; Fig. 3.2). A positive shift at 3810.82 m in the profiles of U, Mo, V, Cr, Fe, and Mn, coupled with a negative shift in the Th/U ratio indicate a shift to anoxic conditions in the middle of the geochemical anomaly. At 3808.08 m, all paleoredox profiles indicate a return to oxic conditions, followed by a smaller positive shift at 3806.53 m. This shift suggests euxinia due to the H_2S-requiring Mo enrichment, however it is likely that there was a smaller abundance of free H_2S than in underlying rocks in the studied succession because of the smaller enrichment in the redox proxies (Algeo and Maynard, 2004; Tribovillard et al., 2004, 2005, 2006).

4.4. Productivity proxies

Productivity proxies aim to examine the trends in photosynthesis in surface waters at the time of deposition. Examining the isotopic signals of $\delta^{13}C_{org}$ and $\delta^{15}N_{air}$ shows a direct relationship to productivity through the preferential uptake of the lighter isotopes by organisms during photosynthesis (e.g., Faure and Mensing, 2004; Hoefs, 2004; Altabet and Francois, 1994; Wang and Azmy, 2020; Piper and Calvert, 2009). Nickel, Cu, and Zn can also be supplied as detritus and/or hydrothermally, however there is no petrographic evidence (such as cement veins) of hydrothermal input in the studied wells (based on core photographs provided by the C-NSOPB).

Productivity proxy profiles show a positive shift within the geochemical anomaly sections of both wells (3916.20 m to 3909.19 m in Thebaud C-74, and 3815.39 m to 3806.53 m in South Desbarres O-76), indicating increased levels of primary productivity and, therefore, an increase in micronutrient delivery. In Thebaud C-74 (Fig. 3.1), a negative shift in $\delta^{13}C_{org}$ and a positive shift in Cu, P, and Zn occurs at 3914.22 m. In South Desbarres O-76 (Fig. 3.2), a

positive shift in Ni, Cu, P, and Zn occurs at 3813.70 m, concurrent with a negative shift in $\delta^{13}C_{org}$. Specifically, the Zn correlated positive peaks (Figs. 3.1 and 3.2) are of importance because productivity consumes Zn without enriching it in seawater, indicating that the micronutrients are supplied to the system via upwelling of OM. Throughout both wells, negative shifts in $\delta^{13}C_{org}$ and positive shifts in micronutrient proxies occur at the same horizons during periods of elevated productivity. This period is associated with a shift in all the redox proxies to more reducing conditions, and low levels of terrigenous input and paleosalinity at the start of the geochemical anomaly.

4.5. Terrigenous input and paleo-salinity proxies

The geochemical composition of siliciclastic sediments is controlled largely by catchment lithology, weathering, transport processes of terrigenous material, as well as diagenetic processes (Dobrzinski et al., 2004; Detian et al., 2019). Commonly used proxies of terrigenous input are Al, Ti, Al/Ti, K/Al, and ∑REEs. (e.g., Piper and Calvert, 2009; Śliwinski et al., 2010; McLennan et al., 1980; Wang and Azmy, 2020).

The terrigenous input proxies within the Thebaud C-74 well (Fig. 3.1) remain relatively low throughout much of the anomaly section but all exhibit a distinct positive shift near the top of the anomaly at 3910.87 m. This suggests that terrigenous input into the basin was negligible for the majority of the anomaly but increased suddenly near the top of the interval. The B/Ga ratio increases from 0.6 at 3912.24 m, to 6.6 at 3910.87 m, at the same level as the increase in terrigenous input proxy profiles (Fig. 3.1). At 3910.87 m, the K/Al ratio also experiences an increase to 0.2, corresponding with the positive excursions observed in the geochemical anomaly. The South Desbarres O-76 well shows distinct enrichments in all terrigenous input proxies from 3815.39 m to 3808.08 m (Fig. 3.2). The B/Ga profile follows the same trend,

exhibiting increases up to 5.3 from 3808.08 m to 3815.39 m. Depletion in B/Ga to 2.2 corresponds to the peak in productivity and redox proxies at 3810.82 m. The K/Al values experience an increase to 0.3 at 3806.53 m, paralleling the positive excursions in Ti and ∑REE. The concurrent enrichment in the terrigenous input, paleosalinity, and clay mineral proxies suggests that terrigenous input was not associated with a freshwater source such as fluvial or groundwater input but could instead be a result of increased evaporation rates and aeolian contribution during a period of aridity and relative sealevel fall (Sabatino et al., 2015; Heimhofer et al., 2008; Barragán et al., 2020).

4.6. Paleoenvironmental Interpretation

The overall analyses of the geochemical anomaly intervals from both the Thebaud C-74 (3916.20 m to 3909.19 m) and South Desbarres O-76 (3815.39 m to 3806.53 m) wells produced similar results and they therefore enable a regional paleoenvironmental interpretation for the Scotian margin. Deposition of sediments was impacted by rift-related tectonism resulting from the Pangea rifting event and the opening of the North Atlantic Ocean, which created relatively more open ocean circulation in the region (Keen and Piper, 1990). Input of micronutrients into the basin via upwelling or adsorption onto OM promoted an increase in primary production in surface waters, indicated by an increase in productivity proxies towards the start of the anomaly in the latest Tithonian (Weston et al., 2012; Ascoli, 2004). This is evidenced by the inverse correlation between the productivity and terrigenous input proxies (Table 3.1; Figs. 3.1 and 3.2), indicating that micronutrient replenishment was unrelated to an influx in terrigenous input and, therefore, was likely the result of increased upwelling during a period of relative sealevel fall. Elevated production drove the shift to anoxic/euxinic conditions, shown by positive correlations between increases in productivity (Ni, Cu, P, Zn) and redox sensitive trace elements (U, V, Mo,

Cr, Fe, and Mn) in both wells (Figs. 3.1 and 3.2). The relationship between productivity and reducing conditions indicates that the high abundance of OM and subsequent decomposition using up oxidative agents was the driver of anoxia, rather than restricted oceanic circulation limiting the replenishment of oxygen. At the top of the anomaly in the uppermost Tithonian, the environment returns to background levels of paleo-productivity and more oxic conditions (Figs. 3.1 and 3.2). Following this, a positive shift in terrigenous input and paleosalinity occurs, correlating with a shift to suboxic/anoxic conditions. An increase in terrigenous input and paleosalinity proxies suggests limited fluvial input, increased rates of evaporation, and increased aeolian contribution, associated with shallow seas and more exposed landmass during relative sealevel fall in a semi-arid/arid paleoclimate. This is supported by high K/Al values which represent the presence of illite, coupled with enriched Ti, which is generally concentrated in the heavy mineral fraction and enriched in fine silty detritus, and can therefore be related to aeolian input associated with an arid climate (Sabatino et al., 2015; Taylor and McLennon, 1985; Emelyanov and Shimkus, 1986; Rachold and Brumsack, 2001; Latta et al., 2006; Heimhofer et al., 2008; Rodríguez-López et al., 2008).

4.7. Global Correlations and Implication for the Jurassic–Cretaceous Boundary

The Thebaud C-74 geochemical anomaly interval (3909.19 m to 3916.20 m) falls within the interpreted Jurassic–Cretaceous boundary interval reported by Ascoli (2004), while the geochemical anomaly within the South Desbarres O-76 well occurs ~35 m lower in the core than the Jurassic–Cretaceous biostratigraphic boundary identified by Weston et al., 2012. Galloway et al. (2020) studied the Volgian Carbon Isotope Excursion (VOICE) in the Sverdrup Basin of Arctic Canada and documented a global negative isotopic excursion event of organic carbon of 4‰ (V-PDB) to a minimum of -30.7‰. The geochemical anomaly in both wells of the current

investigation captures a similar negative shift in organic carbon of 1.5‰ to -26.5‰ in Thebaud C-74, and 2.5‰ to -26.8‰ in South Desbarres O-76 (e.g., Capelli et al., 2020) that can be correlated with the VOICE event (Fig. 4.2). The latest Tithonian was a time of global low sealevel (e.g., Price et al., 2016; Barragan et al., 2020; Martínez-Yáñez et al. 2017; Michalik et al., 1995; Grabowski et al., 2010), extensive anoxic bottom waters and open oceanic circulation (Martínez-Yáñez et al., 2017; Price et al., 2016; Barragan et al., 2020), and semi-arid to arid conditions (Föllmi, 2012; Price et al., 2016; Grabowski et al., 2017; Haq, 2017; Barragán et al., 2020; Capelli et al., 2020). The results of this study are consistent with the isotope stratigraphy profiles of other equivalent successions and their paleoenvironmental conditions. Thus, the Thebaud C-74 and South Desbarres O-76 wells record global events, which allows for the chemostratigraphic global correlation of their $\delta^{13}C_{org}$ record and placing both geochemical anomaly sections at a level equivalent to the biostratigraphically defined uppermost Tithonian (Weston et al., 2012; Ascoli, 2004; Galloway et al., 2020; Koevoets et al., 2016; Hammer et al., 2012; Zakharov et al., 2014; Turner et al., 2019; Fig. 9). The Thebaud C-74 geochemical anomaly interval (3916.20 m to 3909.19 m) falls within the interpreted Jurassic–Cretaceous boundary interval reported by Ascoli (2004), while the geochemical anomaly within the South Desbarres O-76 well occurs ~35 m lower in the core than the Jurassic–Cretaceous biostratigraphic boundary identified by Weston et al., 2012. This variation in correlation might be attributed to some local delay between chemical changes and fossil turnover but further studies may provide more clues.

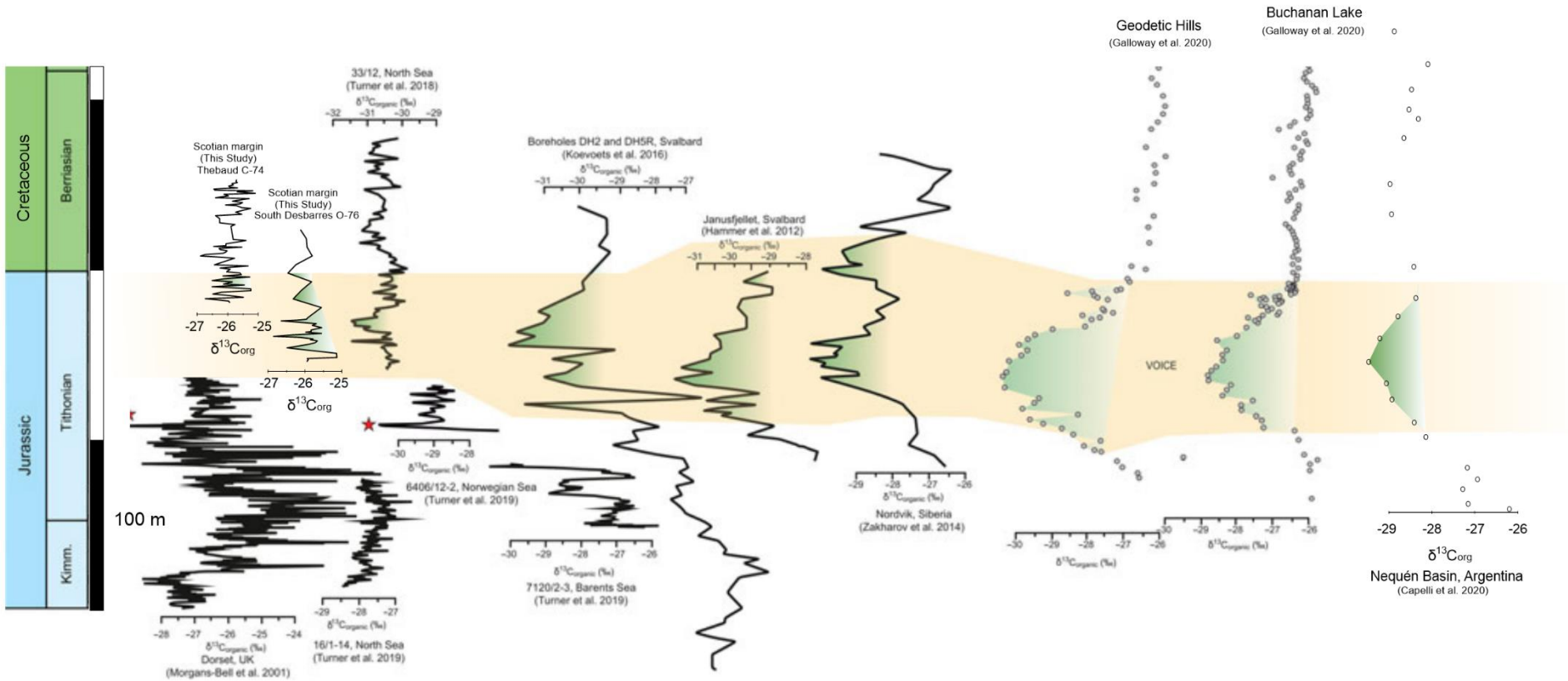

Figure 4.2. Summary of organic isotope data for the Jurassic–Cretaceous from Atlantic, Arctic, and Tethyan sections (modified from Galloway et al., 2020). Red stars indicate levels interpreted as VOICE by Turner et al., 2019.

CHAPTER 5

CONCLUSIONS

The geochemical examination of the Upper Jurassic–Lower Cretaceous interval from the Thebaud C-74 and South Desbarres O-76 wells on the Scotian margin reveals the preservation of near-primary isotopic and trace element signatures that can be used to reconstruct paleoenvironmental conditions. The profiles of paleoredox (TOC/TON, U, V, Mo, Th/U, Cr, Fe, Mn), paleo-productivity ($\delta^{13}C_{org}$, $\delta^{15}N_{air}$, TOC/TON, Ni, Cu, P, Zn), terrigenous input (Al, Ti, Al/Ti, K/Al, ∑REE), and paleosalinity (B/Ga) exhibit a pronounced shift in upper Tithonian strata that are used to identify a geochemical anomaly interval in both wells. Both wells show a transition to euxinic conditions within the anomaly interval associated with an increase in productivity. These changes have poor correlation with terrigenous input proxies, suggesting that replenishment of micronutrient trace elements (Ni, Cu, P, and Zn) that drove increased production was not related to terrigenous influx, but instead sourced from upwelling and adsorption to organic matter in the opening North Atlantic Ocean. The increase in terrigenous input at the end of the geochemical anomaly correlates with an increase in salinity, suggesting aeolian contributions in a semi-arid/arid setting.

Earlier biostratigraphic studies of these wells suggest that the geochemical anomaly occurs in the late Tithonian. The paleoenvironmental interpretations produced from the isotopic and trace elemental analyses of the Thebaud C-74 and South Desbarres O-76 wells align with published global sealevel and paleoclimate studies from the Jurassic–Cretaceous boundary.

REFERENCES

Algeo, T.J. and Lyons, T.W. 2006. Mo-total organic carbon covariation in modern anoxic marine environments: Implications for analysis of paleoredox and paleohydrographic conditions. Paleoceanography, **21 (1)**.

Algeo, T.J., Maynard, J.B., 2004. Trace-element behavior and redox facies in core shales of Upper Pennsylvanian Kansas-type cyclothems. Chemical Geology **206**: 289–318.

Algeo, T.J., and Tribovillard, N. 2009. Environmental analysis of paleoceanographic systems based on molybdenum-uranium covariation. Chemical Geology, **268**: 211–225.

Altabet, M.A. and Francois, R. 1994. Sedimentary nitrogen isotopic ratio as a recorder for surface ocean nitrate utilization. Global Biogeochemical Cycles, **8(1)**: 103–116.

Amoco Canada Petroleum Company Limited and Imperial Oil Limited. 1973. Regional geology of the Grand Banks. Bulletin of Canadian Petroleum Geology, **21**: 479–500.

Anderson, R.F., Fleischer, M.Q., and LeHuray, A.P. 1989. Concentration, oxidation state and particulate flux of uranium in the Black Sea. Geochimica et Cosomochimica Acta, **53**: 2215–2224.

Ascoli, P. 1976. The foraminiferal and ostracod biostratigraphy of the Mesozoic-Cenozoic, Scotian Shelf, Atlantic Canada. *In* First International Symposium on Benthonic Foraminifera of Continental Margins, Part B, Paleoecology and Biostratigraphy: **1.** *Edited by* C.T. Schafer and B.R. Pelletier. Maritime Sediments, Special Publication: 663–771.

Ascoli, P. 1981. Foraminiferal-ostracod Late Jurassic biozonation of the Scotian Shelf. Geological Survey of Canada, Open File **753**: pp. 32.

Ascoli, P., Poag, C. W., and Remane, J. 1984. Microfossil zonation across the Jurassic-Cretaceous boundary of the Atlantic margin of North America. *In* Jurassic-Cretaceous Biochronology and Paleogeography of North America. *Edited by* G.E.G. Westermann. Geological Association of Canada, Special Paper **27**: 31–48.

Ascoli, P. 2004. Report on the Mesozoic foraminiferal and ostracod biostratigraphy and depositional environments of the Mobil *et al.* Thebaud C-74, from 870 to 5150 m (T.D.). Report No. M.R.G.-PAL.07-2004PA, 11 p.

Barragán, R., López-Martínez, R., Chávez-Vergara, B., Núñez-Useche, F., Salgado-Garrido, H., and Merino, A. 2020. Geochemical variations across the Jurassic/Cretaceous boundary in central Mexico. Insights for correlation with Tethyan areas. Journal of South American Earth Sciences, **99**: 102521.

Barss, M.S., Bujak, J.P., and Williams, G.L. 1979. Palynological zonation and correlation of sixty-seven wells, eastern Canada. Geological Survey of Canada, Paper **78-24**: 118 p.

Bartenstein, H. 1967a. Foraminiferal zonation of the Lower Cretaceous in northwest Germany and Trinidad, West Indies – an attempt. Neues Jahrbuch fur Geologie und Palaontologie, Monatshefte, **3**: 187–191.

Bartenstein, H. 1967b. Benthonic index Foraminifera in the Lower Cretaceous of the northern hemisphere between east Canada and northwest Germany. Erdol und Kohl-Erdgas, **29**: 254–256.

Bartenstein, H. 1967c. Practical applicability of a zonation with benthonic foraminifera in the worldwide Lower Cretaceous. Geologie en Mijnhouw, **55**: 83–86.

Beicip-Franlab. 2014. Regional Tectonic Context. *In* Laurentian Sub-Basin Atlas. Offshore Energy Research Association. https://oera.ca/sites/default/files/2019-05/Chapter-03-Regional-Tectonic-Context_BC.pdf

Bennett, W.W., and Canfield, D.E. 2020. Redox-sensitive trace metals as paleoredox proxies: A review and analysis of data from modern sediments. Earth-Science Reviews, **204**: 103175.

Bertine, K.K., and Turekian, K.K. 1973. Molybdenum in marine sediments. Geochimica et Cosmochimica Acta, **37**: 1415–1434.

Bolli, H.M. 1966. Zonation of Cretaceous to Pliocene marine sediments based on planktonic Foraminifera. Boletin Informativo Asociacion Venezolana de Geologia, Mineria Petroleo, **9**: 3–32.

Broecker, W.S., and Peng, T.H. 1982. Tracers in the Sea. Eldigio Press, Colombia University, Palisades, N.Y. 689 p.

Brumsack, H.J. 1989. Geochemistry of recent TOC-rich sediments from the Gulf of California and the Black Sea. Geologische Rundschau, **78**: 851–882.

Bujak, J.P., and Williams, G.L. 1978. Cretaceous palynostratigraphy of offshore southeastern Canada. Geological Survey of Canada, Bulletin **297**: 1–19.

Calvert, S.E., and Pederson, T.F. 1993. Geochemistry of Recent oxic and anoxic marine sediments: Implications for the geological record. Marine Geology, **113(1-2)**: 67–88.

Calvert, S.E., and Piper, D.Z. 1984. Geochemistry of ferromanganese nodules from DOMES site a, Northern Equatorial Pacific: Multiple diagenetic metal sources in the deep sea. Geochimica et Cosmochimica Acta, **48(10)**: 1913–1928.

Canfield, D.E. 1994. Factors influencing organic carbon preservation in marine sediments. Chemical Geology, **114**: 315–329.

Capelli, I.A., Scasso, R.A., Spangenberg, J.E., Kietzmann, D.A., Cravero, F., Duperron, M., and Adatte, T. 2020. Mineralogy and geochemistry of deeply-buried marine sediments of the Vaca Muerta-Quintuco system in the Neuquén Basin (Chacay Melehue section), Argentina: Paleoclimatic and paleoenvironmental implications for the global Tithonian-Valanginian reconstructions. Journal of South American Earth Sciences, **107**: 103103.

Caron, M. 1985. Cretaceous planktic foraminifera. *In* Plankton stratigraphy. *Edited by* H.M. Bolli, J.B. Saunders, and K. Perch-Nielsen. Cambridge University Press, 17-86.

Chaillou, G., Anschutz, P., Lavaux, G., Schäfer, J., Blanc, G., 2002. The distribution of Mo, U, and Cd in relation to major redox species in muddy sediments of the Bay of Biscay. Marine Chemistry, **80**: 41–59.

Cline, J.D., and Kaplan, I.R. 1975. Isotopic fractionation of dissolved nitrate during denitrification in the eastern tropical North Pacific Ocean. Marine Chemistry, **3**: 271–299.

Cremonese, L., Sheilds-Zhou, G., Struck, U., Ling, H.F., Och, L., Chen, X., and Li, D. 2013. Marine biogeochemical cycling during the Early Cambrian constrained by a nitrogen and carbon isotope study of the Xiaotan section, South China. Precambrian Research, **225**: 148–165.

Crusius, J., Calvert, S., Pedersen, T., and Sage, D. 1996. Rhenium and molybdenum enrichments in sediments as indicators of oxic, suboxic, and sulfidic conditions of deposition. Earth and Planetary Science Letters, **145**: 65–78.

Crusius, J., and Thomson, J. 2000. Comparative behavior of authigenic Re, Mo, and U during reoxidation and subsequent long-term burial in marine sediments. Geochimica et Cosmochimica Acta, **64**: 2233–2243.

Davies, E.H. 1985. Palynological analysis of the lower portions (3240-4530) of the Husky-Bow Valley et al. Glooscap C-63 well, Scotia Shelf. Geological Survey of Canada (Atlantic) internal report. Report No. EPGS-PAL.5-85 EHD.

Deptuck, M.E., and Kendell, K.L. 2017. Permo-Triassic Salt Provinces of Europe, North Africa, and the Atlantic Margins. Tectonics and Hydrocarbon Potential, 287–312.

Deptuck, M.E., and Kendell, K.L. 2020. Atlas of 3D seismic surfaces and thickness maps, central and southwestern Scotian Slope. Canada-Nova Scotia Offshore Petroleum Board, Geoscience Open File Report 2020-002MF – 2020-006MF, 51p.

Detian, Y., Daizhao, C., Zhuozhuo, W., Jing, L., Xiangrong, Y., and Bao, Z. 2019. Climatic and oceanic controlled deposition of Late Ordovician–Early Silurian black shales on the North Yangtze platform, South China. Marine and Petroleum Geology, **110**: 112–121.

Dobrzinski, N., Bahlburg, H., Strauss, H., and Zhang, Q.R. 2004. Geochemical climate proxies applied to the Neoproterozoic glacial succession on the Yangtze Platform, South China. *In* Extreme Proterozoic Geology. *Edited by* G. Genkins, M.A.S. McMenamin, C.P. McKay, and I. Sohl. Geochemistry and Climate: 13–32.

Dzyuba, O. S., Izokh, O. P., and Shurygin, B. N. 2013. Carbon isotope excursions in Boreal Jurassic–Cretaceous boundary sections and their correlation potential. Palaeogeography, Palaeoclimatology, Palaeoecology, **381**: 33–46.

Emelyanov, E.M., and Shimkus, K.M. 1986. Geochemistry and Sedimentology of the Mediterranean Sea. Reidel, Dordrecht, The Nederlands. 553 p.

Emerson, S.R., and Huested, S.S. 1991. Ocean anoxia and the concentration of molybdenum and vanadium in seawater. Marine Chemistry, **34**: 177–196.

Erickson, B.E., and Helz, G.R. 2002. Molybdenum (VI) speciation in sulfidic waters. Geochimica et Cosmochimica Acta, **64**: 1149–1158.

Faure, G., and Mensing, T.M. 2004. Isotopes: principles and applications. 3rd ed., Hoboken, N.J., Wiley.

Föllmi, K.B. 2012. Early Cretaceous life, climate and anoxia. Cretaceous Research, **35**: 230–270.

Galloway, J.M., Vickers, M.L., Price, G.D., Poulton, T., Grasby, S.E., Hadlari, T., Beauchamp, B., and Sulphur, K. 2020. Finding the VOICE: organic carbon isotope chemostratigraphy of Late Jurassic – Early Cretaceous Arctic Canada. Geological Magazine, **157**: 1643–1657.

Gao, P., Lia, G., Jia, C., Young, A., Wang, Z., and Wang, T. 2016. Redox variations and organic matter accumulation on the Yangtze carbonate platform during late Ediacaran–early Cambrian: Constraints from petrology and geochemistry. Palaeogeography, Palaeoclimatology, Palaeoecology, **45**: 91–110.

Given, M.M. 1977. Mesozoic and Early Cenozoic geology of offshore Nova Scotia. Bulletin of Canadian Petroleum Geology, **25**: 63–91.

Grabowski, J., Haas, J., Stoykova, K., Wierzbowski, H., and Brański, P. 2017. Environmental changes around the Jurassic/Cretaceous transition: New nannofossil, chemostratigraphic and stable isotope data from the Lókút section (Transdanubian Range, Hungary). Sedimentary Geology, **360**: 54–72.

Hammer, Ø., Collignon, M., and Nakrem, H.A. 2012. Organic carbon isotope chemostratigraphy and cyclostratigraphy in the Volgian of Svalbard. Norwegian Journal of Geology, **92**: 103–112.

Haq, B.U. 2017. Jurassic Sea-Level Variations: A Reappraisal. GSA Today, **28(1)**: 4–10.

Hatch, J.R., and Leventhal, J.S. 1992. Relationship between inferred redox potential of the depositional environment and geochemistry of the Upper Pennsylvanian (Missourian) Stark Shale Member of the Dennis Limestone, Wavaunsee County, Kansas, USA. Chemical Geology, **99**: 65–82.

Heimhofer, U., Adatte, T., Hochuli, P.A., Burla, S., and Weissert, H. 2008. Coastal sediments from the Algarve: Low-latitude climate archive for the Aptian-Albian. International Journal of Earth Sciences, **97**: 785–797.

Helz, G.R., Miller,C.V., Charnock, J.M., Mosselmans, J.L.W., Pattrick, R.A.D., Garner, C.D., and Vaughan, D.J. 1996. Mechanism of molybdenum removal from the sea and its concentration in black shales: EXAFS evidence. Geochimica et Chosmochimica Acta, **60**: 3631–3642.

Hoefs, J. 2004. Stable isotope geochemistry. 5th edition, Berlin; New York, Springer.

Jansa, L.F., and Wade, J.A. 1975. Geology of the continental margin off Nova Scotia and Newfoundland. *In* Offshore Geology of Eastern Canada, Volume 2, Regional Geology. *Edited by* W.J.M. van der Linden and J.A. Wade. Geological Survey of Canada, Paper **74-30**, **2**: 51–106.

Jiang, S.Y., Chen, Y.Q., Ling, H.F., Yang, J.H. Feng, H.Z., and Ni, P. 2006. Trace- and rare-earth element geochemistry and Pb-Pb dating of black shales and intercalated Ni-Mo-PGE-Au sulfide ores in lower Cambrian strata, Yangtze Platform, South China. Miner Deposita, **41**: 453–467.

Jones, B.J., and Manning, A.C. 1994. Comparison of geochemical indices used for the interpretation of palaeoredox conditions in ancient mudstones. Chemical Geology, **111**: 111–129.

Keen, M.J., and Piper, D.J.W. 1990. Geological and historical perspective. *In* Geology of the Continental Margin of Eastern Canada. *Edited by* M.J. Keen and G.L. Williams. Geological Survey of Canada, **2**: 7–30.

Kendall, B., Reinhard, C.T., Lyons, T.W., Kaufman, A.J., Poulton, S.W., and Anbar, A.D. 2010. Pervasive oxygenation along late Archaean Ocean margins. Nature Geoscience, **3**: 647–652.

Kikumoto, R., Tahata, M., Nishizawa, M., Sawaki, Y., Maruyama, S., Shu, D., Han, J., Komiya, T., Takai, K., and Ueno, Y. 2014. Nitrogen isotope chemostratigraphy of the Ediacaran and Early Cambrian platform sequence at Three Gorges, South China. Gondwana Research, **25**: 1057–1069.

Koevoets, M.J., Abay, T.B., Hammer, Ø., and Olaussen, S. 2016. High-resolution organic carbon–isotope stratigraphy of the Middle Jurassic–Lower Cretaceous Agardhfjellet Formation of central Spitsbergen, Svalbard. Palaeogeography, Palaeoclimatology, Palaeoecology, **449**: 266–74.

Labails, C., Olivet, J. L., Aslanian, D., and Roest, W.R. 2010. An alternative early opening scenario for the central Atlantic Ocean. Earth and Science Planetary Letters, **29**: 355–368.

Landing, W.M., and Bruland, K.W. 1987. The contrasting biogeochemistry of iron and manganese in the Pacific Ocean. Geochimica et Cosmochimica Acta, **51**: 29–43.

Latta, D.K., Anastasio, D.J., Hinnov, L.A., Elrick, M., and Kodama, K.P. 2006. Magnetic record of Milankovitch rhythms in lithologically noncyclic marine carbonates. Geology, **34**: 29–32.

Lyons, T.W., and Severmann, S. 2006. A critical look at iron paleoredox proxies: New insights from modern euxinic marine basins. Geochemica et Cosmochimica Acta, **70**: 5698–5722.

MacLean, B.C., and Wade, J.A. 1993. Seismic markers and stratigraphic picks in Scotian Basin wells. *In* East Coast Basin Atlas Series. *Edited* by J.L. Bates. Geological Survey of Canada.

Marillier, F., Keen, C.E., Stockmal, G.S., Quinlan, G., Williams, H., Colman-Sadd, S.P., and O'Brien, S.J. 1989. Crustal structure and surface zonation of the Canadian Appalachians: implications of deep seismic reflection data. Canadian Journal of Earth Sciences, **26**: 305–321.

McIver, N.L. 1972. Cenozoic and Mesozoic stratigraphy of the Nova Scotia Shelf. Canadian Journal of Earth Sciences, **9(1)**: 54–70.

McLennan, S.M., Nance, W.B., and Taylor, S.R. 1980. Rare earth element-thorium correlations in sedimentary rocks, and the composition of the continental crust. Geochimica et Cosmochimica Acta, **44**: 1833–1839.

McLennan, S.M. 2001. Relationships between the trace element composition of sedimentary rocks and upper continental crust. Geochemistry, Geophysics, Geosystems, **2**: 1021 (2000GC000109).

McManus, J., Berelson, W.M., Klinkhammer, G.P., Hammond, D.E., and Holm, C., 2005. Authigenic uranium: Relationship to oxygen penetration depth and organic carbon rain. Geochimica et Cosmochimica Acta, **69**: 95–108.

Morgans-Bell, H.S., Coe, A.L., Hesselbo, S.P., Jenkyns, H.C., Weedon, G.P., Marshall, J.E.A., Tyson, R.V., and Williams, C.J. 2001. Integrated stratigraphy of the Kimmeridge Clay Formation (Upper Jurassic) based on exposures and boreholes in south Dorset, UK. Geological Magazine, **138**: 511–539.

Morse, J.W. and Luther III, G.W. 1999. Chemical influences on trace metal-sulfide interactions in anoxic sediments. Geochimica et Cosmochimica Acta, **63**: 3373–3378.

Mortazavi, M., Moussavi-Harami, R., Mahboubi, A., and Nadjafi, M. 2014. Geochemistry of the Late Jurassic–Early Cretaceous shales (Shurijeh Formation) in the intracontinental Kopet-Dagh Basin, northeastern Iran: implication for provenance, source weathering, and paleoenvironments. Arabian Journal of Geosciences, **7**: 5353–5366.

Mumcuoglu, F., Nachtigall, K.G., Dutton, B.C., and Milne, M.J. 1986. Mobil et al Thebaud C-74 Well History Report. Canada Nova Scotia Offshore Petroleum Board.

Murphy, A.E., Sageman, B.B., Hollander, D.J., Lyons, T.W., and Brett, C.E. 2000. Black shale deposition in the Devonian Appalachian Basin: clastic starvation, episodic water-column mixing, and efficient recycling of biolimiting nutrients. Paleoceanography, **15**: 280–291.

Offshore Energy Technical Research Association. 2011. Play Fairway Analysis Atlas—offshore Nova Scotia. Nova Scotia Department of Energy Report 88-11-0004-01, 349 p. Also available online at: http://www.novascotiaoffshore.com/analysis.

Ohm, U. 1967. Zur Kenntnis dser Gattungen *Reinholdella, Garantella* und *Epistomina* (Foraminifera). Paleontographica, Abt. A, **127**: 103–188.

Pattan, J.N., Mir, I.A., Parthiban, G., Karapurkar, S.G., Matta, V.M., Naidu, P.D., and Naqvi, S.W.A. 2013. Coupling between suboxic condition in sediments of the western Bay of Bengal and southwest monsoon intensification: a geochemical study. Chemical Geology, **343**: 55–66.

Pe-Piper, G., and Jansa, L.F. 1999. Pre-Mesozoic basement rocks offshore Nova Scotia, Canada: new constraints on the accretion history of the Meguma terrane. Geological Society of America Bulletin, **111(12)**: 1773–1791.

Perkins, R.B., Piper, D.Z., and Mason, C.E. 2008. Trace-element budgets in the Ohio/Sunbury shales of Kentucky: Constraints on ocean circulation and primary productivity in the Devonian–Mississippian Appalachian Basin. Palaeogeography, Palaeoclimatology, Palaeoecology, **265**: 14–29.

Piper, D.Z., and Calvert, S.E. 2009. A marine biogeochemical perspective on black shale deposition. Earth Science Review, **95**: 63–96.

Piper, D.Z., and Perkins, R.B. 2004. A modern vs. Permian black shale - the hydrography, primary productivity, and water-column chemistry of deposition. Chemical Geology, **206**: 177–197.

Poulton, S.W., Fralick, P.W., and Canfield, D.E. 2010. Spatial variability in oceanic redox structure 1.8 billion years ago. National Geographic, **3**: 486–490.

Price, G.D., Főzy, I., and Pálfy, J. 2016. Carbon cycle history through the Jurassic – Cretaceous boundary: A new global $\delta^{13}C$ stack. Palaeogeography, Palaeoclimatology, Palaeoecology, **451**: 46–61.

Quan, T.M., Wright, J.D., and Falkowski, P.G. 2013. Co-variation of nitrogen isotopes and redox states through glacial-interglacial cycles in the Black Sea. Geochimica et Cosmochimica Acta, **112**: 305–320.

Rachold, V., and Brumsack, H.J. 2001. Inorganic geochemistry of Albian sediments from the Lower Saxony Basin NW Germany: palaeoenvironmental constraints and orbital cycles. Palaeogeography, Palaeoclimatology, Palaeoecology, **174**: 121–143.

Remane, J. 1991. The Jurassic-Cretaceous boundary: Problems of definition and procedure. Cretaceous Research, **12(5)**: 447–453.

Rimmer, S.M. 2004. Geochemical paleoredox indicators of Devonian–Mississippian black shales, central Appalachian basin (USA). Chemical Geology, **206**: 373–391.

Rodríguez-López, J.P., Meléndez, N., de Boer, P.L., and Soria, A.R. 2008. Aeolian sand sea development along the mid-Cretaceous western Tethyan margin (Spain): erg sedimentology and palaeoclimate implications. Sedimentology, **55**: 1253–1292.

Sabatino, N., Coccioni, R., Manta, D.S., Baudin, F., Vallefuoco, M., Traina, A., and Sprovieri, M. 2015. High-resolution chemostratigraphy of the late Aptian–early Albian oceanic anoxic event (OAE 1b) from the Poggio le Guaine section (Umbria-Marche Basin, central Italy). Palaeogeography, Palaeoclimatology, Palaeoecology, **426**: 319–333.

Schenk, P.E. 1971. Southeastern Atlantic Canada, Northwestern Africa, and Continental Drift. Canadian Journal of Earth Sciences, **8**: 1218–1251.

Schnetger, B., Brumsack, H.J., Schale, H., Hinrichs, J., and Dittert, L. 2000. Geochemical characteristics of deep-sea sediments from the Arabian Sea: a high-resolution study. Deep-Sea Res. II, **47**: 2735–2768.

Schoepfer, S.D., Shen, J., Wei, H., Tyson, R.V., Ingall, E., and Algeo, T.J. 2014. Total organic carbon, organic phosphorus, and biogenic barium fluxes as proxies for paleomarine productivity. Earth-Science Reviews, **149**: 23–52.

Scott, R. W. 2019. Jurassic–Cretaceous boundary bioevents and magnetochrons: A stratigraphic experiment. Cretaceous Research, **100**: 97–104.

Shembilu, N.C., and Azmy, K. 2022. Trace element variations across Middle–Upper Cambrian carbonates: Implications for the paleoenvironment of eastern Laurentia. Marine and Petroleum Geology, **135**: 105385.

Sibuet, J.C., Rouzo, S., and Srivastava, S. 2011. Annex 13: plate tectonic reconstructions and paleo-geographic maps of the central and north Atlantic oceans. *In* OETR (Offshore Energy Technical Research Association), Play Fairway Analysis Atlas – offshore Nova Scotia. Nova Scotia Department of Energy Report **88-11-0004-01**: pp. 349.

Sine, G., Ellsworth, W., and Donnely, D. 1984. Shell Petrocan et al South Desbarres O-76 Well History Report. Canada Nova Scotia Offshore Petroleum Board.

Śliwiński, M.G., Whalen, M.T., and Day, J. 2010. Trace element variations in the middle Frasnian punctata zone (late Devonian) in the Western Canada Sedimentary Basin - changes in oceanic bioproductivity and paleoredox spurred by a pulse of terrestrial afforestation? Geologica Belgica, **4**: 459–482.

Swanson, M. T. 1986. Pre-existing fault control for Mesozoic basin formation in eastern North America. Geology, **14**: 419–422.

Taylor, S.R., and McLennan, S.M. 1985. The continental crust: its composition and evolution. An examination of the geochemical record preserved in sedimentary rocks. Blackwell, Oxford, 312 p.

Tennant, J. P., Mannion, P. D., Upchurch, P., Sutton, M. D., and Price, G. D. 2017. Biotic and environmental dynamics through the Late Jurassic–Early Cretaceous transition: Evidence for protracted faunal and ecological turnover. Biological Reviews, **92(2)**: 776–814.

Tribovillard, N., Riboulleau, A., Lyons, T., and Baudin, F. 2004. Enhanced trapping of molybdenum by sulfurized organic matter of marine origin as recorded by various Mesozoic formations. Chemical Geology, **213**: 385–401.

Tribovillard, N., Ramdani, A., and Trentesaux, A. 2005. Controls on organic accumulation in upper Jurassic shales of northwestern Europe as inferred from trace-metal geochemistry. *In* The Deposition of Organic-Carbon-Rich Sediments: Models, Mechanisms, and Consequences. *Edited by* N, Harris. SEPM Special Publications, **82**: 145–164.

Tribovillard, N., Algeo, T.J., Lyons, T., and Riboulleau, A. 2006. Trace metals as paleoredox and paleoproductivity proxies: an update. Chemical Geology, **232**: 12–32.

Tribovillard, N., Algeo, T.J., Baudin, F., and Riboulleau, A. 2012. Analysis of marine environmental conditions based on molybdenum-uranium covariation – Applications to Mesozoic paleoceanography. Chemical Geology, **324**: 46–58.

Tripathy, G.R., Hannah, J.L., Stein, H.J., and Yang, G. 2014. Re-Os age and depositional environment for black shales from the Cambrian-Ordovician boundary, Green Point, western Newfoundland. Geochemistry, Geophysics, Geosystems, **14(4)**: 1021–1037.

Turner, H.E., Batenburg, S.J., Gale, A.S., and Gradstein, F.M. 2019. The Kimmeridge Clay Formation (Upper Jurassic–Lower Cretaceous) of the Norwegian Continental Shelf and Dorset, UK: a chemostratigraphic correlation. Newsletters on Stratigraphy, **52**: 1–32.

Van Helden, B.G.T. 1986. Dinoflagellate cysts at the Jurassic-Cretaceous boundary, offshore east Newfoundland, eastern Canada. Palynology, **10**: 181–200.

Van Hinte, J.E. 1976. A Jurassic time scale. American Association of Petroleum Geologists Bulletin, **60**: 489–497.

Vindušková, O., Jandová, K., and Frouz, J. 2019. Improved method for removing siderite by *in situ* acidification before elemental and isotope analysis of soil organic carbon. Journal of Plant Nutrition and Soil Science, **182**: 82–91.

Wada, E. 1980. Nitrogen isotope fractionation and its significance in biogeochemical processes occurring in marine environments. *In* Isotope Marine Chemistry. *Edited by* E.D. Goldberg and Y. Horive: 375–398.

Wade, J.A. 2012. *Regional Geoscience Overview*. CNSOPB. https://callforbids.cnsopb.ns.ca/2012/01/overview/regional-geoscience/regional-geoscience-overview.html

Wade, J.A., MacLean, B.C., and Williams, G.L. 1995. Mesozoic and Cenozoic stratigraphy, eastern Scotian Shelf: new interpretations. Canadian Journal of Earth Sciences, **32**: 1462–1473.

Wade, J.A., and MacLean, B.C. 1990a. The geology of the southeastern margin of Canada. *In* Geology of the continental margin of eastern Canada. *Edited by* M.J. Keen and G.L. Williams. Geological Survey of Canada, Geology of Canada, **No. 2**: 167–238.

Wade, J.A., and MacLean, B.C. 1990b. The geology of the southeastern margin of Canada. Part 2: Aspects of the geology of the Scotian Basin from recent seismic and well data. *In* Geology of the continental margin of eastern Canada. *Edited by* M.J. Keen and G.L. Williams. Geological Survey of Canada, Geology of Canada, **No. 2**: 190–238.

Wang, L., and Azmy, K. 2020. Palaeoenvironmental changes in slope carbonates across the Late Cambrian–Early Ordovician in western Newfoundland. Geological Journal, **55**: 3451–3463.

Wehrly, B., and Stumm, W. 1989. Vanadyl in natural waters: adsorption, and hydrolysis promote oxygenation. Geochimica et Cosmochimica Acta, **53**: 69–77.

Wei, W., and Algeo, T.J. 2020. Elemental proxies for paleosalinity analysis of ancient shales and mudrocks. Geochimica et Cosmochimica Acta, **287**: 341–366.

Weston, J.F., MacRae, R.A., Ascoli, P., Cooper, M.K.E., Fensome, R.A., Shaw, D., and Williams, G.L. 2012. A revised biostratigraphic and well-log sequence-stratigraphic framework for the Scotian Margin, offshore eastern Canada. Canadian Journal of Earth Sciences, **49**: 1417–1462.

Wignall, P.B., and Myers, K.J. 1988. Interpreting the benthic oxygen levels in mudrocks: a new approach. Geology, **16**: 452–455.

Wignall, P.B., and Twitchett, R.J. 1996. Oceanic anoxia and the end Permian mass extinction. Science, **272**: 1155–1158.

Wignall, P.B., Zonneveld, J.P., Newton, R.J., Amor, K., Sephton, M.A., and Hartley, S. 2007. The end Triassic mass extinction record of Williston Lake, British Columbia. Palaeogeography, Palaeoclimatology, Palaeoecology, **253**: 385–406.

Williams, G.L. 1975. Dinoflagellate and spore stratigraphy of the Mesozoic-Cenozoic, offshore eastern Canada. *In* Offshore Geology of Eastern Canada, Volume 2, Regional Geology. *Edited by* W.J.M. van der Linden and J.A. Wade; Geological Survey of Canada, Paper **74-30**, **2**: 107–161.

Williams, G.L. 1979. The Appalachian Orogen in Canada. Canadian Journal of Earth Sciences, **16**: 792–807.

Williams, G.L., Ascoli, P., Barss, M.S., Bujak, J.P., Davies, E.H., Fensome, R.A., and Williamson, M.A. 1990. Biostratigraphy and related studies. *In* Geology of the Continental Margin of Eastern Canada. *Edited by* M.J. Keen and G.L. Williams. Geological Survey of Canada, Geology of Canada, **No. 2**: 89–137.

Wimbledon, W. A. P. 2008. The Jurassic-Cretaceous boundary: An age-old correlative enigma. Episodes, **31(4)**: 423–428.

Yamaguchi, K.E., Ogurim, K., Ogawa, N.O., Sakai, S., Hirano, S., Kitazato, H., and Ohkouchi, N. 2010. Geochemistry of modern carbonaceous sediments overlain by a water mass

showing photic zone anoxia in the saline meromictic Lake Kai-ike, southwest Japan: I. Early diagenesis of organic carbon, nitrogen, and phosphorous. Palaeogeography, Palaeoclimatology, Palaeoecology, **294**: 72–82.

Zakharov, V.A., Rogov, M.A., Dzyuba, O.Z., Žák, K., Košt'ák, M., Pruner, P., Skupien, P., Chadima, M., Mazuch, M., and Nikitenko, B.L. 2014. Palaeoenvironments and palaeoceanography changes across the Jurassic/Cretaceous boundary in the Arctic realm: case study of the Nordvik section (north Siberia, Russia). Polar Research, **33**: 19714.

Zheng, Y., Anderson, R.F., van Geen, A., Kuwabara, J. 2000. Authigenic molybdenum formation in marine sediments: a link to pore water sulfide in the Santa Barbara Basin. Geochimica et Cosmochimica Acta, **64**: 4165–4178.

Zheng, Y., Anderson, R.F., van Geen, A., and Fleisheir, M.Q. 2002a. Preservation of non-lithogenic particulate uranium in marine sediments. Geochimica et Cosmochimica Acta, **66**: 3085–3092.

Zheng, Y., Anderson, R.F., van Geen, A., and Fleisheir, M.Q. 2002b. Remobilization of authigenic uranium in marine sediments by bioturbation. Geochimica et Cosmochimica Acta, **66**: 1759–1772.

Zhou, L., Wignall, P.B., Su, J., Feng, Q., Xie, S., Zhao, L., and Huang, J. 2012. U/Mo ratios and $\delta^{95/95}$Mo as local and global redox proxies during mass extinction events. Chemical Geology, **324**: 99–107.Algeo, T.J., and Lyons, T.W. 2006. Mo-total organic carbon covariation in modern anoxic marine environments: Implications for analysis of paleoredox and paleohydrographic conditions. Paleoceanography, **21(1)**.

APPENDICES

Appendix A: Sample IDs, core, depth, and isotopic and elemental geochemical compositions of the Thebaud C-74 and South Desbarres O-76 wells. Samples within the geochemical anomaly interval are highlighted.

Sample ID	Core	Depth	U (ppm)	Mo (ppm)	V (ppm)	Cr (ppm)	Fe (ppm)	Mn (ppm)	B/Ga	K/Al
NL-Th1-2	1	-3857.05	3.21	1.70	175	164	66868	591	4.48	0.23
NL-Th1-6	1	-3858.46	2.82	1.72	181.3	143.5	80456.2	726.6	3.98	0.09
NL-Th1-10	1	-3859.83	2.47	1.24	161	123.4	67039.2	289.3	4.07	0.07
NL-Th1-14	1	-3861.00	2.35	2.21	130.6	126.5	69432.5	156.5	4.01	0.22
NL-Th1-20	1	-3863.76	0.62	1.27	57	117.8	30404.6	327.1	4.06	0.10
NL-Th1-27	1	-3869.03	0.99	0.8	53.5	112.9	29716.1	269.6	4.67	0.12
NL-Th1-33	1	-3873.12	0.37	0.74	29.3	20.5	9904.2	1935.2	5.92	0.18
NL-Th2-3	2	-3877.28	1.51	2.01	44.7	65.3	33682.4	82.9	4.67	0.18
NL-Th2-7	2	-3881.35	1.53	0.3	43	131	20836	174	3.27	0.14
NL-Th2-9	2	-3883.34	1.26	0.36	36.3	94.7	15943.4	218.1	5.28	0.16
NL-Th3-1	3	-3890.85	4.1	2.72	187.4	149	83583.9	181	3.92	0.10
NL-Th4-5	4	-3893.34	4.27	2.79	162.9	148.9	35419.6	384.2	3.64	0.30
NL-Th4-6	4	-3894.32	2.68	1.1	77	77	62708	1315	3.83	0.25
NL-Th4-7	4	-3894.76	2.5	1.8	100	85	41379	458	1.95	0.22
NL-Th4-11	4	-3895.96	3.35	2.72	145.4	134.9	52716.4	646.3	4.44	0.09
NL-Th4-13	4	-3896.64	3.2	1.84	152	130.4	55951.7	848.1	4.33	0.29
NL-Th4-17	4	-3898.05	4.96	5.54	168.3	162.1	49481.7	399.4	3.87	0.31
NL-Th4-19	4	-3898.69	1.94	2.75	89.7	84.1	53084.5	219.5	3.99	0.09
NL-Th4-21	4	-3899.39	3.15	1.69	178.8	141.5	31235.8	177.9	3.95	0.10
NL-Th4-23	4	-3900.21	2.49	1.54	151	133.8	56438.5	723.5	4.29	0.09
NL-Th4-25	4	-3900.97	2.8	1.27	158	137.2	38266.7	351.6	4.84	0.15
NL-Th4-27	4	-3901.53	4.11	3.28	137.3	116.5	45838.1	244.8	3.09	0.25
NL-Th4-29	4	-3902.22	4.53	2.27	121.3	119	34556.1	172.5	3.69	0.25
NL-Th5-1	5	-3905.23	0.75	0.97	34.3	48.5	20481.9	393.1	4.04	0.14
NL-Th5-2	5	-3905.92	2.37	8.52	146.2	119.6	81446.1	475.6	3.08	0.23
NL-Th5-3	5	-3907.04	1.14	1.31	59.8	72.5	21117.9	147.7	3.17	0.19
NL-Th5-4	5	-3907.77	0.94	0.39	50	43.7	35203.9	122.8	3.18	0.15
NL-Th5-6	**5**	**-3909.19**	**1.67**	**0.5**	**81**	**80**	**51152**	**107**	**2.51**	**0.20**
NL-Th6-2	**6**	**-3910.87**	**4.07**	**1.71**	**218.7**	**194.2**	**67175.5**	**345.2**	**6.56**	**0.20**
NL-Th6-3	**6**	**-3911.57**	**1.14**	**0.4**	**40**	**80**	**25887**	**40**	**3.10**	**0.10**
NL-Th6-4	**6**	**-3912.24**	**2.22**	**7.9**	**85**	**80**	**136206**	**461**	**0.34**	**0.21**
NL-Th6-6	**6**	**-3914.22**	**0.58**	**5.5**	**21**	**116**	**19063**	**571**	**2.60**	**0.10**
NL-Th6-8	**6**	**-3916.2**	**0.41**	**0.67**	**21**	**34.3**	**17316.2**	**347.5**	**-**	**0.09**
NL-Th6-10	6	-3917.66	0.39	0.74	23	52.5	20874.9	513.8	-	0.08
NL-Th6-12	6	-3919.92	1.25	0.5	55	71	28819	45	2.04	0.09
NL-Th6-14	6	-3921.85	0.56	0.59	31.9	48	14930.5	120.3	3.46	0.07
NL-Th6-16	6	-3923.72	0.62	1.1	25	55	14745	263	4.91	0.08
NL-Th6-18	6	-3925.86	0.79	0.69	50.6	58.7	46007.2	348.2	2.12	0.09

Sample ID	Core	Depth	Ni (ppm)	Cu (ppm)	P (ppm)	Zn (ppm)	Al (ppm)	Ti(ppm)	∑REE
NL-Th1-2	1	-3857.05	70.0	30.1	1111	172	135678	10069	317.17
NL-Th1-6	1	-3858.46	71.6	33.3	1192.6	147.2	376363	9044.6	333.09
NL-Th1-10	1	-3859.83	64.2	26.4	806.9	144.9	377863.9	8329.4	279.15
NL-Th1-14	1	-3861.00	47.4	16.9	612.5	97.7	85381.1	8912.8	270.31
NL-Th1-20	1	-3863.76	28.8	10.6	242.1	143.7	28592.5	2638.2	105.47
NL-Th1-27	1	-3869.03	16.2	9.2	368.1	68.5	29233.7	4505.4	139.75
NL-Th1-33	1	-3873.12	4.6	1.8	140.9	17.4	11771.1	770.6	75.54
NL-Th2-3	2	-3877.28	34.2	20.9	515.8	48.1	50974.1	4571.7	187.54
NL-Th2-7	2	-3881.35	18	6.3	361	91	27787	5394	137.59
NL-Th2-9	2	-3883.34	15.8	6.1	391.9	88.4	26445.2	4297.2	133.81
NL-Th3-1	3	-3890.85	67.2	28	1032.6	167.7	344285.7	12966.6	477.49
NL-Th4-5	4	-3893.34	57.6	24.9	695.9	161.4	125205.7	12480.1	434.53
NL-Th4-6	4	-3894.32	28.2	11.8	585	111	65647	6802	277.62
NL-Th4-7	4	-3894.76	42.5	28.1	588	145	107544	6612	299.96
NL-Th4-11	4	-3895.96	51.1	28.8	1115.2	248.2	383823.1	10030	408.82
NL-Th4-13	4	-3896.64	47.9	28.2	987.2	173.8	127876.6	9926.9	405.26
NL-Th4-17	4	-3898.05	55.4	35.3	844.9	230	125146.3	13580.1	539.82
NL-Th4-19	4	-3898.69	41.6	18.2	563	144.1	150150	5216.4	297.82
NL-Th4-21	4	-3899.39	55.2	38.6	571.8	92.4	456272.1	8629.3	374.53
NL-Th4-23	4	-3900.21	55.2	29.8	655.9	90.1	526178.1	7864.2	290.19
NL-Th4-25	4	-3900.97	54.9	35	497.6	800.5	533606	8112.5	334.53
NL-Th4-27	4	-3901.53	60.1	28.3	732.6	341	126886.4	9897.1	560.08
NL-Th4-29	4	-3902.22	41.1	20.7	786.4	214.4	111997.8	10350.1	562.59
NL-Th5-1	5	-3905.23	24	4.7	332	136.4	28450.7	3077.9	77.72
NL-Th5-2	5	-3905.92	95.2	24.9	704.3	88.9	105064.5	10064.7	280.67
NL-Th5-3	5	-3907.04	23	8.5	416.3	34.1	42299.7	5694.6	133.27
NL-Th5-4	5	-3907.77	23.7	4.7	308.5	34.7	38393.3	3024.3	109.49
NL-Th5-6	**5**	**-3909.19**	**36**	**10.5**	**287**	**28**	**49062**	**4873**	**180.66**
NL-Th6-2	**6**	**-3910.87**	**71.9**	**21.6**	**684.7**	**67.3**	**577966.4**	**14143.1**	**834.94**
NL-Th6-3	**6**	**-3911.57**	**17.5**	**2.7**	**282**	**60**	**25321**	**3900**	**106.7**
NL-Th6-4	**6**	**-3912.24**	**234.8**	**50**	**383**	**85**	**44682**	**5633**	**188.77**
NL-Th6-6	**6**	**-3914.22**	**12.6**	**17.2**	**195**	**1940**	**12855**	**1675**	**39.56**
NL-Th6-8	**6**	**-3916.2**	**9.9**	**2.7**	**203.5**	**71.2**	**15381.3**	**1586.5**	**46.9**
NL-Th6-10	6	-3917.66	12.5	4.3	299.9	40.9	15060.6	1364.4	56.03
NL-Th6-12	6	-3919.92	42.4	6	614	50	48046	5301	138.88
NL-Th6-14	6	-3921.85	10.6	2.8	314.4	34.7	26732.2	3106.4	59.52
NL-Th6-16	6	-3923.72	18.8	5.8	323	67	18436	2287	71.76
NL-Th6-18	6	-3925.86	24.7	7.5	528.1	42.8	37740.1	3752.3	91.02

Sample ID	Core	Depth	U (ppm)	Mo (ppm)	V (ppm)	Cr (ppm)	Fe (ppm)	Mn (ppm)	B/Ga	K/Al
NL-SDC-1	C	-3750	2.14	1.75	104.7	125.8	45229.1	625.8	4.79	0.33
NL-SDC-2	C	-3755	1.81	1.17	92.5	110.6	33257.3	376.2	4.39	0.12
NL-SDC-3	C	-3760	1.26	1.97	52.8	86.3	32308.6	453.2	4.59	0.32
NL-SDC-4	C	-3765	2.48	1.5	106	130	35887	430	4.56	0.25
NL-SDC-5	C	-3770	1.96	1.1	78	87	31257	532	1.79	0.32
NL-SDC-6	C	-3775	2.68	4.9	116	140	44423	671	4.01	0.27
NL-SDC-7	C	-3780	1.05	2	39	52	32830	840	5.80	0.37
NL-SDC-8	C	-3785	2.31	1.57	103.2	134.5	32762.5	245.2	4.72	0.27
NL-SDC-9	C	-3790	2.42	1.2	97	144	37786	254	5.06	0.25
NL-SDC-10	C	-3795	1.6	1.09	85.3	95.5	32206.8	829.4	4.13	0.33
NL-SD1-1	1	-3800.87	8.15	4.2	284	368	70694	246	5.45	0.31
NL-SD1-3	1	-3802.3	0.25	0.13	16.2	20.1	7765	71.4	2.84	0.42
NL-SD1-5	1	-3804.34	1.93	0.65	47.9	89	23377.1	74.5	4.67	0.34
NL-SD1-7	**1**	**-3806.53**	**6.02**	**5.11**	**226.8**	**327.9**	**86493.2**	**195.7**	**4.32**	**0.33**
NL-SD2-1	**2**	**-3808.08**	**4.8**	**2.14**	**206.3**	**281.1**	**51688.2**	**200**	**5.32**	**0.11**
NL-SD2-6	**2**	**-3810.82**	**2.88**	**2.18**	**91.1**	**264.3**	**85037.2**	**210.9**	**2.15**	**0.30**
NL-SD2-9	**2**	**-3812.31**	**3.33**	**2.36**	**133.4**	**178.6**	**68144.4**	**271.4**	**4.80**	**0.32**
NL-SD2-12	**2**	**-3813.70**	**3.79**	**2.8**	**205**	**180**	**53055**	**378**	**4.78**	**0.25**
NL-SD2-16	**2**	**-3815.39**	**3.19**	**3.16**	**210.2**	**176.9**	**56011.7**	**353.8**	**5.21**	**0.10**
NL-SD2-22	2	-3818.40	1.97	0.5	106	111	32048	134	4.21	0.28
NL-SD2-32	2	-3823.96	2.55	2.29	178.6	129.4	61458.3	164.8	4.70	0.26
NL-SD2-34	2	-3825.25	3.66	1.6	184	179	35637	165	5.13	0.32

Sample ID	Core	Depth	Ni (ppm)	Cu (ppm)	P (ppm)	Zn (ppm)	Al (ppm)	Ti (ppm)	∑REE
NL-SDC-1	C	-3750	54.7	21.3	872	91.9	65211.7	7394.2	168.17
NL-SDC-2	C	-3755	42.1	14.6	686	78.1	141549.9	5893.4	161.13
NL-SDC-3	C	-3760	32.2	15.5	439.1	41.3	33597.3	3987.3	91.71
NL-SDC-4	C	-3765	45.7	15.2	723	92	80263	6392	157.78
NL-SDC-5	C	-3770	38.4	13.9	620	66	44300	4750	135.34
NL-SDC-6	C	-3775	63.2	31.4	898	448	74498	6474	224.52
NL-SDC-7	C	-3780	20.2	7.9	541	22	17462	2253	84.3
NL-SDC-8	C	-3785	53.7	17.8	577.2	51.4	70570.6	6711.9	188.05
NL-SDC-9	C	-3790	57.1	16.3	542	62	78985	7007	148.62
NL-SDC-10	C	-3795	27.9	12.6	800.8	32.8	41012.4	4967.5	154.67
NL-SD1-1	1	-3800.87	131.7	35.3	2034	110	160361	25591	644.49
NL-SD1-3	1	-3802.3	6.6	2.9	109.7	20.5	14428.6	675	42.45
NL-SD1-5	1	-3804.34	27.1	7.7	291.9	27.5	21333.7	5573.7	198.9
NL-SD1-7	**1**	**-3806.53**	**173.9**	**39**	**928.5**	**181.7**	**92695.9**	**20701.1**	**493.04**

NL-SD2-1	**2**	**-3808.08**	**76.8**	**28.1**	**866.4**	**250.1**	**329888.9**	**14799.5**	**414.75**
NL-SD2-6	**2**	**-3810.82**	**162.8**	**29.4**	**616.8**	**63.7**	**24581.4**	**8209.7**	**205.54**
NL-SD2-9	**2**	**-3812.31**	**69.1**	**21.1**	**1171.2**	**73.1**	**85401.5**	**11065.7**	**316.05**
NL-SD2-12	**2**	**-3813.70**	**101**	**29.2**	**1203**	**96**	**150853**	**10544**	**313.25**
NL-SD2-16	**2**	**-3815.39**	**148.2**	**34.8**	**910.3**	**98.6**	**425408.4**	**9731.5**	**350.83**
NL-SD2-22	2	-3818.40	52.5	13.2	682	50	71553	5920	197.51
NL-SD2-32	2	-3823.96	146.3	22.4	924.7	113.2	82670.1	8805.6	331.46
NL-SD2-34	2	-3825.25	72.5	25.8	879	85	100981	10879	300.66

Sample ID	Core	Depth	$\delta^{13}C_{org}$ (‰)	$\delta^{15}N_{air}$ (‰)	TOC (wt. %)	TON (wt. %)
NL-Th1-2	1	-3857.05	-25.71	9.02	1.94	0.22
NL-Th1-4	1	-3857.75	-25.73	10.09	1.42	0.21
NL-Th1-6	1	-3858.46	-25.69	9.99	1.83	0.22
NL-Th1-8	1	-3859	-25.86	9.07	1.25	0.21
NL-Th1-10	1	-3859.83	-25.82	10.79	1.69	0.24
NL-Th1-12	1	-3860.49	-25.97	7.53	1.02	0.04
NL-Th1-14	1	-3861	-25.93	10.1	0.63	0.09
NL-Th1-15	1	-3861.55	-25.68	-17.16	0.41	0.14
NL-Th1-16	1	-3861.83	-26.15	-12.94	0.3	0.04
NL-Th1-17	1	-3862.26	-26.45	-13.5	0.63	0.51
NL-Th1-18	1	-3862.76	-26.42	-16.55	0.27	0.1
NL-Th1-19	1	-3863.11	-25.18	-18.37	0.88	0.13
NL-Th1-20	1	-3863.76	-25.69	-6.16	0.11	0.08
NL-Th1-21	1	-3864.59	-25.1	-17.77	0.1	0.09
NL-Th1-22	1	-3865.06	-26.12	-19.76	0.25	0.12
NL-Th1-23	1	-3866.07	-25.98	7.52	0.37	0.04
NL-Th1-24	1	-3867.07	-26.4	-11.31	0.49	0.11
NL-Th1-25	1	-3867.63	-25.3	-7.8	4.53	0.23
NL-Th1-26	1	-3867.99	-25.46	-17.28	0.7	0.11
NL-Th1-27	1	-3869.03	-25.84	18.79	0.67	0.02
NL-Th1-28	1	-3869.87	-25.52	-7.48	2.38	0.14
NL-Th1-29	1	-3870.66	-25.61	-6.58	2.69	0.15
NL-Th1-30	1	-3871.19	-26.07	12.24	0.24	0.05
NL-Th1-31	1	-3871.58	-25.7	-7.45	3.67	0.19
NL-Th1-32	1	-3872.73	-25.53	-5.71	3.7	0.15
NL-Th1-33	1	-3873.12	-25.25	4.19	3.16	0.01
NL-Th2-1	2	-3875.27	-25.73	10.71	0.98	0.16
NL-Th2-2	2	-3876.53	-25.54	-6.87	2.26	0.24
NL-Th2-3	2	-3877.28	-26.4	11.07	0.28	0.21
NL-Th2-5	2	-3879.03	-26.26	7.49	0.1	0.06

NL-Th2-7	2	-3881.35	-26.26	7.54	0.13	0.02
NL-Th2-8	2	-3882.33	-25.76	10.3	0.12	0.05
NL-Th2-9	2	-3883.34	-25.9	9.47	-	0.04
NL-Th3-1	3	-3890.85	-25.82	8.76	0.88	0.24
NL-Th4-1	4	-3891.41	-25.4	10.26	0.15	0.09
NL-Th4-5	4	-3893.34	-26.06	10.52	1.62	0.25
NL-Th4-6	4	-3894.32	-26.06	9.69	1.12	0.09
NL-Th4-7	4	-3894.76	-26.46	10.27	0.45	0.12
NL-Th4-9	4	-3895.24	-25.54	11.67	1.13	0.23
NL-Th4-11	4	-3895.96	-26.28	11.61	1.12	0.26
NL-Th4-13	4	-3896.64	-26.24	10.75	1.09	0.25
NL-Th4-15	4	-3897.28	-26.02	8.13	1.05	0.25
NL-Th4-17	4	-3898.05	-26.07	8.85	2.07	0.33
NL-Th4-19	4	-3898.69	-26.16	12.23	0.32	0.1
NL-Th4-21	4	-3899.39	-26.74	11.49	0.41	0.28
NL-Th4-23	4	-3900.21	-26.89	6.97	-	0.02
NL-Th4-25	4	-3900.97	-26.16	10.32	0.44	0.3
NL-Th4-27	4	-3901.53	-25.78	9.11	2.58	0.24
NL-Th4-29	4	-3902.22	-25.91	11.03	1.08	0.21
NL-Th5-1	5	-3905.23	-26.44	7.17	0.22	0.03
NL-Th5-2	5	-3905.92	-25.34	9.1	3.17	0.32
NL-Th5-3	5	-3907.04	-26.25	12.9	0.22	0.06
NL-Th5-4	5	-3907.77	-25.92	-1.76	0.36	0.16
NL-Th5-6	5	-3909.19	-26.04	13.37	0.29	0.13
NL-Th6-1	6	-3909.9	-25.6	5.99	1.59	0.01
NL-Th6-2	6	-3910.87	-25.56	-0.81	1.19	0.36
NL-Th6-3	6	-3911.57	-26.16	9.85	2.33	0.03
NL-Th6-4	6	-3912.24	-25.28	4.6	4.65	0.4
NL-Th6-5	6	-3913.17	-26.13	5.73	0.22	0.01
NL-Th6-6	6	-3914.22	-26.51	9.55	0.23	0.02
NL-Th6-7	6	-3915	-25.85	5.83	0.21	0.01
NL-Th6-8	6	-3916.2	-26.14	4.12	0.14	0.04
NL-Th6-9	6	-3916.77	-25.47	6.45	0.2	0.01
NL-Th6-10	6	-3917.66	-26.51	6.29	0.22	0.01
NL-Th6-11	6	-3919.01	-25.24	9.76	2.92	0.16
NL-Th6-12	6	-3919.92	-25.24	12.75	0.13	0.03
NL-Th6-13	6	-3920.86	-26.21	12.06	-	0.02
NL-Th6-14	6	-3921.85	-26.49	-22.77	0.04	0.07
NL-Th6-15	6	-3922.78	-25.93	6.17	0.08	0.01
NL-Th6-16	6	-3923.72	-25.49	6.21	0.12	0.01
NL-Th6-17	6	-3924.49	-26.73	9.84	0.59	0.21

NL-Th6-18	6	-3925.86	-23.67	9.43	0.26	0.08
NL-Th6-19	6	-3926.61	-24.77	11.39	0.43	0.08

Sample ID	Core	Depth	$\delta^{13}C_{org}$ (‰)	$\delta^{15}N_{air}$ (‰)	TOC (wt. %)	TON (wt. %)
NL-SDC-1	C	-3750	-26.11	10.16	1.51	0.22
NL-SDC-2	C	-3755	-25.96	10.89	1.33	0.13
NL-SDC-3	C	-3760	-25.94	8.63	0.98	0.1
NL-SDC-4	C	-3765	-25.8	11.12	1.43	0.14
NL-SDC-5	C	-3770	-26.24	9.58	1.18	0.1
NL-SDC-6	C	-3775	-26.46	7.29	2.3	0.37
NL-SDC-7	C	-3780	-25.82	7.85	0.37	0.02
NL-SDC-8	C	-3785	-26.09	8.98	0.72	0.18
NL-SDC-9	C	-3790	-26.32	9.23	0.48	0.13
NL-SDC-10	C	-3795	-25.55	3.21	0.42	0.06
NL-SD1-1	1	-3800.87	-25.92	8.98	3.34	0.32
NL-SD1-2	1	-3801.8	-25.96	10.35	2.98	0.36
NL-SD1-3	1	-3802.3	-26.23	4.05	0.1	0.03
NL-SD1-4	1	-3802.73	-26.64	8.71	0.11	0.02
NL-SD1-5	1	-3804.34	-25.69	6.15	0.87	0.05
NL-SD1-6	1	-3805.33	-25.8	-1	2.23	0.37
NL-SD1-7	1	-3806.65	-25.54	3.33	6.07	0.3
NL-SD1-8	1	-3807.53	-25.73	6.18	7.34	0.43
NL-SD2-1	2	-3808.08	-25.83	7.84	2.36	0.26
NL-SD2-3	2	-3808.89	-25.83	10.4	3.21	0.37
NL-SD2-4	2	-3809.25	-25.97	2.71	1.05	0.17
NL-SD2-5	2	-3810.05	-25.55	8.1	4.51	0.28
NL-SD2-6	2	-3810.82	-26.34	5.74	0.88	0.13
NL-SD2-7	2	-3811.7	-26.84	6.41	0.09	0.08
NL-SD2-9	2	-3812.31	-26.13	-0.9	1.34	0.26
NL-SD2-11	2	-3813.22	-25.78	-4.96	1.52	0.35
NL-SD2-12	2	-3813.7	-25.84	5.42	1.62	0.31
NL-SD2-14	2	-3814.38	-25.66	9.97	2.31	0.17
NL-SD2-16	2	-3815.39	-25.72	7.46	2.4	0.42
NL-SD2-18	2	-3816.27	-25.88	4.53	1.97	0.3
NL-SD2-22	2	-3818.4	-26.48	8.11	0.5	0.18
NL-SD2-29	2	-3821.53	-25.14	9.56	6.95	0.48
NL-SD2-32	2	-3823.96	-25.13	-6.23	8.27	0.46
NL-SD2-33	2	-3824.65	-25.93	11.08	0.36	0.05
NL-SD2-34	2	-3825.25	-25.91	4.48	1.26	0.29
NL-SD2-36	2	-3826.17	-25.94	5.67	1.71	0.28